HHS Public Access

Author manuscript

J Control Release. Author manuscript; available in PMC 2021 November 10.

Published in final edited form as:

J Control Release. 2020 November 10; 327: 266–283. doi:10.1016/j.jconrel.2020.07.024.

Nanoformulation of CCL21 Greatly Increases Its Effectiveness as an Immunotherapy for Neuroblastoma

Brittany J. Poelaert[a], **Svetlana Romanova**[b], **Shelby M. Knoche**[a], **Madeline T. Olson**[a], **Bailee H. Sliker**[a], **Kaitlin Smits**[a], **Brittney L. Dickey**[a], **Alexandra E. J. Moffitt-Holida**[a], **Benjamin T. Goetz**[a], **Nuzhat Khan**[a], **Lynette Smith**[c,d], **Hamid Band**[a,c], **Aaron M. Mohs**[b,c,f], **Donald W. Coulter**[c,e], **Tatiana K. Bronich**[b,c], **Joyce C. Solheim**[a,c,f,g,*]

[a]Eppley Institute for Research in Cancer and Allied Diseases, University of Nebraska Medical Center, Omaha NE 68198

[b]Department of Pharmaceutical Sciences and Center for Drug Delivery and Nanomedicine, College of Pharmacy, University of Nebraska Medical Center, Omaha NE 68198

[c]Fred and Pamela Buffett Cancer Center, University of Nebraska Medical Center, Omaha NE 68198

[d]Department of Biostatistics, University of Nebraska Medical Center, Omaha NE 68198

[e]Department of Pediatrics, University of Nebraska Medical Center, Omaha NE 68198

[f]Department of Biochemistry and Molecular Biology, University of Nebraska Medical Center, Omaha NE 68198

[g]Department of Pathology and Microbiology, University of Nebraska Medical Center, Omaha NE 68198

Abstract

Neuroblastoma is the most commonly diagnosed extracranial solid tumor in children. The patients with aggressive metastatic disease or refractory/relapsed neuroblastoma currently face a dismally low chance of survival. Thus, there is a great need for more effective therapies for this illness. In previous studies, we, as well as others, showed that the immune cell chemoattractant C-C motif chemokine ligand 21 (CCL21) is effective as an intratumoral therapy able to slow the growth of cancers. In this current study, we developed and tested an injectable, slow-release, uniform, and optimally loaded alginate nanoformulation of CCL21 as a means to provide prolonged intratumoral treatment. The alginate-nanoformulated CCL21, when injected intratumorally into mice bearing neuroblastoma lesions, significantly prolonged survival and decreased the tumor growth rate compared to CCL21 alone, empty nanoparticles, or buffer. Notably, we also observed complete tumor clearance and subsequent full protection against tumor rechallenge in 33% of

[*]Correspondence to Joyce C. Solheim, Eppley Institute for Research in Cancer and Allied Diseases, University of Nebraska Medical Center, 986805 Nebraska Medical Center, Omaha, NE USA 68198 (jsolheim@unmc.edu).

nanoformulated CCL21-treated mice. Greater intratumoral presence of nanoformulated CCL21, compared to free CCL21, at days 1 and 2 after treatment ended was confirmed through fluorescent labeling and tracking. Nanoformulated CCL21-treated tumors exhibited a general pattern of prolonged increases in anti-tumor cytokines and relatively lower levels of pro-tumor cytokines in comparison to tumors treated with CCL21 alone or buffer only. Thus, this novel nanoformulation of CCL21 is an effective treatment for neuroblastoma, and may have potential for the delivery of CCL21 to other types of solid tumors in the future and as a slow-release delivery modality for other immunotherapies.

Keywords

cancer; CCL21; immunotherapy; nanomedicine; nanoparticle; neuroblastoma; nanoformulation

1. Introduction

Intratumoral administration of C-C motif chemokine ligand 21 (CCL21) can potentially induce tumor infiltration by immune cells and cause systemic inhibition of tumor growth, as shown by our studies in pancreatic and mammary cancer models [1–2]. Results from other research groups have also strongly supported CCL21's anti-tumor activity and its potential as a cancer therapy [3–12]. CCL21, also known as secondary lymphoid tissue chemokine or 6Ckine, is normally expressed by high endothelial venules in secondary lymphoid organs, lymph nodes, and the spleen [13]. CCL21 functions as a chemoattractant for mature dendritic cells (DCs), naïve and memory T cells, natural killer (NK) cells, and natural killer T (NKT) cells, which all express the CCL21 receptor (chemokine receptor 7) [14–17]. The co-localization of antigen-stimulated DCs and naïve T cells, as facilitated by CCL21 chemotactic gradients, allows for T cell activation and induction of an immune response [15]. Alongside the demonstration of its chemotactic abilities, CCL21 has also been shown to increase apoptotic resistance and endocytic capabilities of DCs, improve the survival and cytotoxic activity of T cells used in adoptive immunotherapy, and enhance chemo-sensitivity in tumors when used in a multimodal approach [18–22]. The varied capabilities of CCL21 (chemotaxis of immune effector cells, subsequent evocation of immune responses, augmentation of chemotherapy effectiveness, and improved functionality of DCs and cytotoxic T cells) strongly support CCL21's development and use as a therapeutic agent.

Sustained drug release can contribute to the rate and extent of availability of therapeutic agents, which are crucial factors for treatment efficacy. The aim of any drug delivery system is to provide a therapeutic amount of the drug to specific sites within the body in order to maintain the desired drug concentration over a period of time, thus leading to a more pronounced effect. Drug delivery systems that allow sustained release provide promising approaches for better control over the concentration of therapeutic agents. Such tactics not only allow for preserving the therapeutic efficacy of the treatment agent(s) but can also potentially reduce the frequency of drug administration or the fluctuation of drug levels, thereby resulting in a shorter treatment period. Drug delivery systems are rapidly evolving to provide novel treatment strategies with reduced dosage and administration frequency, improved control over treatment release, and enhanced therapeutic efficacy.

In this context, encapsulation of CCL21 into implantable devices or particulate systems as chemokine depots may provide better control over the duration of its chemotactic gradient. Liposomes and poly(lactide-co-glycolide) (PLGA) microspheres or nanoparticles are the most extensively explored as particulate platforms for local cytokine delivery [23]. While a number of studies demonstrated the promise of these strategies for anticancer immunotherapies, the challenge for these formulations is related to relatively low protein loading. In this study, we have designed novel alginate nanoparticles that combine a drug-encapsulating matrix with the beneficial effects of a sustained release formulation. Alginate, a derivative of brown seaweed, is a naturally occurring polysaccharide that contains 1–4'-linked β-D-mannuronic acid (M) and α-L-guluronic acid (G) residues that form alternating homo-polymeric block regions. Alginate has a negative charge at neutral pH, and in the presence of divalent cations such as calcium ions (Ca^{2+}) that bind specifically to blocks of G residues, it forms a cross-linked gel [24]. This polymer has been approved by the Food and Drug Administration as a component in various products for use in the treatment of wounds, tissue engineering, and drug delivery [24–26]. Properties such as biocompatibility, mild gelation conditions, low cost, and minimal toxicity allow for its extensive medical usage [27]. Additionally, alginate-based microspheres have previously been tested for encapsulation and *in vitro* release of chemokines, including CCL21 [28].

We then used this novel alginate-based nanoformulation to optimize the delivery of CCL21 for the treatment of neuroblastoma, which is a cancer of the sympathetic nervous system that occurs predominantly in early childhood and represents 6% of all pediatric cancer cases [29]. In children, neuroblastoma is the most common extracranial solid tumor diagnosed, and it results in 12–15% of all pediatric cancer-related deaths [30–33]. Neuroblastoma staging takes into account DNA ploidy, histological features, genetic alterations, and clinical data (as specified by the International Neuroblastoma Risk group) to define classes of risk as being low, intermediate, or high [34–35]. Patients with high-risk disease have a low 5-year survival rate of <50% [34–36]. Aggressive treatment strategies utilizing radiation, chemotherapy, surgery, and hematopoietic stem cell transplantation are severely limited in their abilities to prolong the lives of children diagnosed with advanced stage neuroblastoma or relapse/recurrent disease, and for patients who have relapsed the 5-year survival is only 20% [37–42]. Survivors of neuroblastoma have been shown to experience long-term toxicities (secondary malignancies, failure to grow, hearing loss, hypothyroidism, renal toxicities, and ovarian failure) and even increased mortality as a result of their treatments [43–47].

Thus, innovative treatment strategies for neuroblastoma are needed. In general, immunotherapies tend to have milder side effects than chemotherapies or radiation therapies, which makes them attractive for use in pediatric patients. Several studies have shown neuroblastoma cells to be susceptible to killing by immune cells, such as natural killer cells and T cells [48–56]. Immunotherapies to facilitate the attraction of these immune cells to neuroblastomas are options to investigate as new strategies to treat neuroblastoma patients. Providing sustained release of CCL21 in the neuroblastoma tumor environment should allow the continuance of an influx of immune cells over a prolonged period of time, and thereby improve the immunological and therapeutic effects beyond what might be attainable with CCL21 alone. We have designed this CCL21 nanoformulation in such a way that it can

potentially be used to treat tumors at internal sites in patients, because the nanoparticles are small enough (<300 nm) to avoid clogging the small gauge needles and tubing that are used for drug delivery to internal organs. In the study reported here, we have tested the hypothesis that intratumoral administration of alginate-based nanoformulation of CCL21 will result in improved inhibition of tumor growth and longer survival of neuroblastoma-bearing mice, due to sustained release of CCL21 and infiltration of immune cells able to induce a systemic antitumor immune response.

2. Materials and methods

2.1. Materials

CCL21 was acquired from Peprotech (Rocky Hill, NJ) and cytochrome c was supplied by Calbiochem (San Diego, CA). Lyophilized recombinant murine CCL21 (stored at −20°C) was reconstituted in either sterile phosphate-buffered saline buffer control (PBS) or purified water (Barnstead/Thermolyne Nanopure Water System, Dubuque, TX). Reconstituted CCL21 was stored at 4°C until use. PBS was purchased from GE Healthcare Life Sciences (Marlborough, MA). The following materials were purchased from Sigma-Aldrich (St. Louis, MO): alginic acid sodium salt, Pluronic F127, CCL21 ELISA, collagenase A, and DNase I. Calcium chloride ($CaCl_2$), 40 μm strainers, 15 mL conical vials, 50 mL conical vials, ammonium-chloride-potassium (ACK) buffer, trypan blue, Optimal Cutting Temperature Compound, charged microscope slides, and LIVE/DEAD Fixable Blue Dead Cell Stain was purchased from Thermo Fisher Scientific (Hampton, NH). Protamine sulfate was acquired from MP Biomedicals LLC (Santa Ana, CA). Formvar/silicon monoxide-coated 200 mesh copper grids were purchased from Ted Pella Inc. (Redding, CA). The GloQube glow discharge unit was from Quorum Technologies (East Sussex, UK) while NanoVan was from Nanoprobes (New York, NY). The 50 kDa Float-A-Lyzer dialysis tubing was purchased from Spectrum Laboratories Inc. (Rancho Dominguez, CA). The Amicon 3000 Da protein concentrators were bought from Millipore (Burlington, MA). The Neuro2a cell line was acquired from the ATCC (Manassas, VA). Media reagents, which include Dulbecco's Modified Eagle Medium (DMEM), sodium pyruvate, penicillin, streptomycin, L-glutamine, and MEM Non-Essential Amino Acids, were obtained from Life Technologies (Carlsbad, CA). Fetal bovine serum was purchased from Atlanta Biologicals (Flowery Branch, GA). The IR800CW dye was purchased from LI-COR (Lincoln, NE). Antibodies were purchased from Miltenyi Biotec (Bergisch Gladbach, Germany). The Proteome Profiler Mouse Cytokine Array Kit, Panel A was obtained from R&D Systems (Minneapolis, MN).

2.2. Formulation of the nanoparticles: overview and detailed procedure

Alginate nanoparticles were prepared from diluted alginate stock solution (alginic acid sodium salt with medium viscosity, pH 8.0) by inducing a pre-gel formation with calcium counter ions, followed by polyelectrolyte complex formation with protamine sulfate (Fig. 1). Protamine sulfate, which functions as a polycation in this system, allows for the formation of the polyelectrolyte complex with opposite charged alginate polysaccharides, thus stabilizing the alginate pre-gel nucleus into individual sponge-like nanoparticles. Pluronic F127 is a hydrophilic, nontoxic copolymer that is widely used as a pharmaceutical excipient. Biocompatibility, bioadhesion, adaptability, thermosensitivity, and ability to stabilize and

protect cargo have all promoted the use of Pluronic F127 as a component in many therapeutic modalities, including nanogels or nanocontainers, microvesicle nancompexes, and engineered tissues [57–62]. In these alginate nanoparticles, Pluronic F127 was used as a matrix-stabilizing agent that permits sustained drug release. Thus, in total, the alginate nanoparticles include several components conducive to structural stabilization: low concentration of alginate polysaccharide stock, Ca^{2+} ions (aqua solution of calcium chloride), a polycation (protamine sulfate), and the F127 pluronic block copolymer.

To begin the nanoformulation procedure, alginate nanoparticles were prepared using standard ionotropic gelation processes. In brief, an alginate aqueous solution (1.0 mL of a 1.5 mg/mL solution) was gently mixed at 4°C with 250 μg (for a 6:1 alginate : protein ratio) or 25 μg (for a 60:1 alginate : protein ratio) of cytochrome c or CCL21. For formulations that included Pluronic F127, 100 μl of a 10% w/w solution of Pluronic F127 was added to the alginate mixture and stirred for an additional 10 minutes following an initial period (5 minutes) of mild agitation at 4°C 300 rpm. The stirring speed was adjusted to 800 rpm before 125 μl of a 2 mg/mL solution of $CaCl_2$ was added drop by drop to induce gelation of the alginate mixture. After 30 min of the gelation process, protamine sulfate (75 μl of a 2 mg/mL solution) was incorporated and the resultant, slightly opalescent dispersions were stirred for an additional 1 h (800 rpm, 4°C) to complete formation of the nanoparticles. Simultaneously, with each batch of protein-containing nanoparticles, empty nanoparticles (at the same concentrations of alginate, $CaCl_2$, protamine sulfate, and Pluronic F127) were prepared as a control. All nanoparticles, with or without protein cargo, were stored at 4°C until use.

2.3. Characterization of the nanoparticles

Protein-loaded and empty alginate nanoparticles were characterized by dynamic light scattering (DLS) for intensity-weighted z-averaged hydrodynamic diameter (D_{eff}, nm) and polydispersity index (PDI), and by Nanoparticle Tracking Analysis for number-weighted diameter and particle concentration. DLS measurements were performed in PBS at 25°C and at a fixed 173° scattering angle using a Nano ZS Zetasizer (Malvern Instruments, Worcestershire, UK). Software provided by the manufacturer (Zetasizer software Version 7.11, Malvern Panalytical) was used to calculate the D_{eff} and PDI. In addition, the hydrodynamic diameter of the particles was measured using the field flow fractionation technique (FFF) coupled to an online DLS detector (Eclipse DualTech Asymmetric FFF System, Wyatt Technology, Santa Barbara, CA). Particle dispersion in PBS (1.35 mg/mL) was injected through a 50 μL loop into AS4 channel (350 μm spacer W type, 10 kDa regenerated cellulose membrane) and PBS was used as a mobile phase. After a focus step at 1 mL/minute, a gradient elution exerting a cross-flow decreasing exponentially between 3 mL/minute and 0 mL/minute was applied for 9 minutes (detector flow: 0.8 mL/minute). The hydrodynamic diameter of the particles was determined in the elution window between 5 and 7 minutes using the Astra 7.1.3 software provided by the manufacturer. For Nanoparticle Tracking Analysis, samples were diluted 10X with PBS and measurements were done with a NanoSight NS300TM (Malvern Instruments) at 25°C. Five individual videos (60 sec duration each) for every sample were recorded and analyzed using the Nanoparticle Tracking Analysis software Version 3.2.

The morphology of the alginate nanoparticles was studied using transmission electron microscopy (TEM). Samples for TEM imaging were spotted onto formvar/silicon monoxide-coated 200 mesh copper grids. Grids were glow discharged for 60 seconds at 20 μA with a GloQube glow discharge unit prior to use. Samples were negatively stained with NanoVan and examined on a Tecnai G2 Spirit TWIN (FEI, Hillsboro, OR) operating at an accelerating voltage of 80 kV. Images were acquired digitally with an AMT (Woburn, MA) digital imaging system. Cryo-transmission electron microscopy (cryo-TEM) measurements were performed on alginate NPs prepared at a concentration of 2 mg/ml in distilled water. Sample preparation for cryo-TEM was done in a temperature and humidity-controlled chamber using a fully automated vitrification robot (Vitrobot, FEI Co., Hillsboro, OR). A thin aqueous film of nanoparticle solution was formed on a carbon grid at 22°C and at 100% relative humidity. The thin film was rapidly vitrified by shooting the grid into liquid ethane. The grids with the vitrified thin films were transferred into the microscope chamber. Micrographs were taken using a FEI Tecnai F30 microscope operating at 300 kV, equipped with Gatan 626 cryo-holder with α +/− 70° tilt range and ability to keep samples at −170°C during imaging.

The morphology of the alginate nanoparticles was also analyzed by atomic force microscopy (AFM). Samples for AFM imaging were prepared by depositing 5 μL of an aqueous dispersion of nanoparticles (concentration 2.5×10^{-3} mg/mL) onto positively charged 1-(3-aminopropyl) silatrane mica (APS-mica) surfaces for 2 min, followed by surface drying under argon atmosphere. AFM imaging was performed in air with a Multimode NanoScope IV system (Veeco, Santa Barbara, CA) operating in a typing mode and silicon probes (spring constant of 42 N/m). Femtoscan software (Advanced Technologies Center, Moscow, Russia) was used to characterize nanoparticle dimensions.

To measure the encapsulation efficiency and loading capacity for cytochrome c, 1.0 mL of each formulation was centrifuged at 10,000 rpm (30,000 × g) for 30 min at 4°C in a Beckman Coulter Optima L-90K ultracentrifuge, the supernatant was carefully collected without disturbing the pellet, and absorbance values were measured with the NanoDrop spectrophotometer to determine the amount of free cytochrome c in the supernatant. The concentration of cytochrome c in the supernatant was determined by UV/Vis (absorbance max at Soret band, 409 nm) and calculated using a standard curve. The protein encapsulation efficiency (EE, %) was calculated as the percentage of the encapsulated amount of the protein relative to the initial given amount, and loading capacity (LC, %) was calculated as the percentage of the amount of encapsulated protein relative to the total weight of loaded alginate nanoparticles. Thus, for calculation of encapsulation efficiency, the following formula was used: encapsulation efficiency (EE%) = [mass of protein in alginate nanoparticles/mass of initial protein added] × 100%. To calculate the loading capacity, this formula was used: loading capacity (LC%) = [mass of protein in alginate nanoparticles/mass of the protein-loaded alginate nanoparticles] × 100%. An enzyme-linked immunosorbent assay (ELISA) was used to determine the efficiency of CCL21 loading into the nanoparticles. Fresh samples of alginate nanoparticles with CCL21 cargo were centrifuged at 35,000 rpm (122,000 × g) in a Beckman Coulter Optima L-90K ultracentrifuge for 40 min at 4°C. After centrifugation, the supernatant samples were tested by ELISA per the manufacturer’s protocol, using a Molecular Devices SpectraMax microplate reader with

comparison to known levels of CCL21 in a standard curve (established with recombinant murine CCL21).

2.4. Analysis of in vitro protein release

A membrane dialysis method was used *in vitro* to simulate cytochrome c or CCL21 release *in vivo*. The nanoparticle formulation (1 mL of each formulation) was placed into a 50 kDa Float-A-Lyzer dialysis tube, submerged in a 50 mL conical vial containing 45 mL of PBS (pH 7.4), and incubated at 37°C with constant shaking at 100 rpm. At specified time points, an aliquot of PBS was removed from the outer volume of the dialysis apparatus and replaced with an equivalent amount of fresh PBS to maintain a constant volume in the tube. The dialysate samples were concentrated by 60 min centrifugation at 4°C, 1,200 rpm (314 × g) in a Sorvall Legend X1R centrifuge (Thermo Scientific) to approximately 500 μL using an Amicon 3000 Da protein concentrator before analysis. The amount of cytochrome c released at each time point was determined by measuring absorbance at 450 nm with a NanoDrop spectrophotometer (Thermo Fisher Scientific). ELISA was used to quantify the amount of CCL21 released over time from the nanoparticles during dialysis. For either cytochrome c or CCL21, the amount of protein released from the alginate nanoparticles was expressed as a percentage of the total loaded protein and plotted as a function of time.

2.5. Tumor cell injections and treatments of tumor-bearing mice

Neuro2a cells (clonal derivative of a spontaneous tumor, C1300) were thawed from a bank of low passage, parental stock vials and subcultured no more than 5 times before use *in vivo* with a syngeneic mouse (A/J) strain [63–64]. The Neuro2a cells were cultured in Dulbecco's Modified Eagle Medium (DMEM) supplemented with the following additives: 1 mM sodium pyruvate, 100 units/mL penicillin and 100 μg/mL streptomycin, 2 mM L-glutamine, 100X MEM Non-Essential Amino Acids, along with 10% v/v heat inactivated fetal bovine serum.

Female A/J mice, 4 weeks of age, were purchased from Jackson Laboratories (Bar Harbor, ME) and acclimated to their new, pathogen-free environment for 2 weeks before study initiation. All experiments were performed according to the Institutional Animal Care and Use (IACUC) protocol. The A/J mice were subcutaneously injected with 1 X 10^6 Neuro2a cells/100 μL PBS in the lower right flank. Upon detection of palpable tumors (volume ≥ 50 mm^3), which occurred approximately 9–12 days post-implantation, the mice were divided into blinded treatment or control groups ($n \geq 6$ mice/group per experimental replicate), with the groups having matched average tumor volumes. The nanoformulated CCL21 treatment or controls were administered intratumorally twice daily (in the morning and evening for 2 consecutive days (days 0 and 1), providing 6 μg of CCL21/25 μL, or 6 μg of CCL21 in nanoformulation/25 μL per dose, or an equal amount of empty nanoparticles/25 μL, or an equal volume (25 μL) of buffer. Visual quartering of the tumor allowed for equal distribution of injection sites and treatment delivery. Fig. S1 depicts the strategy used throughout the *in vivo* studies performed. The mice were monitored for 54 days, at least 3 times weekly, with documentation of tumor growth and overall health (weight, food/water consumption, and any indications of reduced mobility or responsiveness). Survival time indicates the number of days until tumors reach a volume of 1000 mm^3 (per IACUC requirements) and the mice

were euthanized. Tumor-free mice (post 54 days) that had been treated with nanoformulated CCL21 and undergone complete tumor regression, along with treatment-naïve, age- and sex-matched control mice, were rechallenged on the opposite hind flank (left flank) with 1 X 10^6 Neuro2a cells/100 μL PBS, and were subsequently monitored for tumor development. Tumor volume (in mm^3) was determined using caliper measurements (in 2 perpendicular directions) and the following formula: (tumor $width^2$) X (tumor length/2).

2.6. Fluorescent tagging of alginate nanoparticles and CCL21

CCL21 amino groups were labeled with IR800 dye. In brief, 500 μg (1.05 μmole of amino groups) were labeled with NHS-active form of IR800 dye (6.13 μg, 0.5% mol. in 2 mL water). The reaction was stirred overnight at room temperature before the unconjugated dye was removed by dialyses against water. Protein recovery was achieved through lyophilization and stored at −20°C prior to use. The labeled CCL21 was then used in the nanoformulation process as described above.

2.7. Fluorescence imaging and analysis of tagged nanoparticles and/or CCL21 in vivo

A/J mice received intratumoral injections of the nanoparticles, free CCL21, or buffer control (as detailed above). Images *in vivo* were collected on the Pearl® Trilogy Small Animal Imaging System over a 120-hour time course (pre-injection and at 24, 48, 72, 96, and 120 hours following treatment initiation). Upon conclusion of the study, tumors, various organs (kidney, spleen, and liver) and draining lymph nodes were collected from the euthanized mice for imaging. The images were analyzed using Image Studio software version 5.0 (LI-COR Biosciences; Lincoln, NE). Briefly, a region of interest was manually drawn around the tumor or necropsied organ or lymph node to obtain the mean fluorescent signal. Differences between treatment groups were calculated with GraphPad Prism software version 7.03.

2.8. Fluorescent microscopy analysis of tumors treated with tagged nanoparticles and/or CCL21

Necropsied tissues were embedded in Optimal Cutting Temperature Compound (OCT) and stored at −20°C until processing for histology. Tissues were cut into 10 μm sections using a cryostat (Leica, Buffalo Grove, IL), and mounted on charged microscope slides. The slides were imaged with an Olympus DP80 Digital Camera and CellSense Dimension Software in the 800 nm channel to detect the presence of the nanoparticle and CCL21 (respectively).

2.9. Flow cytometric investigation of immune cell infiltration into tumors

Direct immunofluorescent staining was used to analyze immune cell populations in tumor samples. Neuro2a tumor-bearing female mice (n >5 mice per group) were treated intratumorally with CCL21 only, nanoformulated CCL21, or buffer control using the same treatment regimen described in Section 2.5 and diagrammed in Fig. S1. Following excision, each tumor was gently rinsed 2–3 times with sterile PBS. On the last rinse, most of the PBS was removed, such that less than 1 mL of PBS remained. The tumor was minced into small pieces using 2 sterile razor blades, transferred to a 15 mL conical with digestion media (DMEM + 10% FBS, 2 mg/mL Collagenase A, and 0.25 units/mL DNase I), and incubated for 45 minutes at 37°C with constant shaking. The tumor mixture was then transferred to a

pre-moistened sterile 40 μm cell strainer attached to a 50 mL sterile conical tube and macerated through the strainer using the back of a syringe plunger. The cell strainer was then washed 3 times with ~5 mL of sterile PBS per wash before centrifugation of the tube at 1,500 rpm (453 × g), 4°C, for 5 min in an Eppendorf 5810R centrifuge. The supernatant was decanted, and the pellet was resuspended in 2 mL of ammonium-chloride-potassium (ACK) buffer to lyse erythrocytes. After incubation of the suspension in the ACK buffer at room temperature for 5 min, 30 mL of PBS was added and the suspension was centrifuged at 1,500 rpm (453 × g), 4°C, for 5 min. The cells were resuspended in PBS, and cell number and viability were determined by mixing a small aliquot of the cell suspension with 0.4% trypan blue and counting the cells in the mixture on a hemocytometer. Viability of the cells was determined to be at least 95% prior to flow cytometry.

Throughout the staining process, the cells and reagents were kept on ice and protected from light. The cells were stained with antibodies against surface markers of macrophages, DCs, NK cells, NKT cells, T cells, and B cells (see Fig. S2 and Table S2 for antibody lists, dilutions, and clone information). Cells were also stained with LIVE/DEAD Fixable Blue Dead Cell Stain following the manufacturer's protocol to assess cell viability. In brief, the digested tumor samples were resuspended in 500 μL of PBS before being dispersed equally (100 μL of tumor cell suspension per panel) into the 4 immunoprofiling panels with the additional 100 μL being incorporated into a pooled sample for use in control wells (i.e. unstained cells, fluorescents minus one, etc.). The cells were washed 3x with 100 μL PBS and centrifuged at 1,500 rpm (453 × g), 4°C, for 5 min. The cells were then resuspended in 100 μL of the antibody cocktail and incubated for 30 minutes at 4°C, protected from light. After incubation, the cells were washed 3x with100 μL PBS and centrifuged at 1,500 rpm (453 × g), 4°C, for 5 min prior to fixation in 1% paraformaldehyde in PBS. The stained cells were processed using the BD LSRII flow cytometer (Franklin Lakes, NJ) and analyzed by FlowJo software (Ashland, OR). The percentage of each lymphocyte population within a tumor was calculated as % CD45 = (number of cells positive for a specific marker)/(total number of cells) X 100. The percentages of T cells, DCs, NK cells, and macrophages were calculated as % marker = (number of cells marker positive)/(number of live cells) X 100.

2.10. Multiplex analysis of cytokine profiles in treated neuroblastoma tumors

To investigate differences in cytokine profiles, at the time of necropsy a 2 mm × 2 mm tumor biopsy was acquired from each mouse that had been treated with nano-CCL21, free CCL21, or buffer only following the treatment regimen described in Section 2.5 and diagrammed in Fig. S1). Each biopsied tumor was plated in 1 well of a 12-well plate in 2 mL of base media (DMEM) and incubated at 37°C for 72 hours to allow for cytokine secretion. After incubation, the samples were centrifuged at 1,500 rpm (453 × g) for 5 minutes at 4°C followed by collection of the culture supernatant. The culture supernatant samples were then stored at −20°C. Prior to analysis, the culture supernatant samples were thawed and approximately 300 μL of culture supernatant from each mouse was pooled into a total volume of 2 mL per time point per treatment group. Each pooled culture supernatant sample was then concentrated using the Amicon Ultra-2 Ultracel-3 (Sigma) centrifugal filter unit per the manufacturer's protocol by loading it into the Ultra-2 device and centrifuging for 40 minutes at 4,454 rpm (4,000 × g). The concentrated culture supernatant sample was

recovered with an additional centrifugation at 2,227 rpm (1,000 × g) for 2 minutes. The concentrated samples were then used to determine cytokine profiles for each treatment group.

The concentrated, pooled tumor culture supernatant from each treatment group (buffer control, nanoformulated CCL21, and CCL21 alone) at day 2 and day 7 post treatment were analyzed via the Proteome Profiler Mouse Cytokine Array Kit, Panel A (R&D Systems) as directed by the manufacturer. Briefly, a mixture of concentrated culture supernatant and antibody cocktail solution was prepared and incubated for 1 hour at room temperature followed by incubation with a membrane overnight at 4°C on a shaking platform. The membranes were washed 3x for 10 minutes each before incubation in a Streptavidin-HRP solution for 30 minutes at room temperature on a rocking platform. Another series of washes was performed before visualization using the provided Chemi Reagent solution and Bio-rad Gel Doc Documentation system.

2.11. Statistical analysis

Linear Mixed Models analysis, IBM SPSS Statistics version 25 (Armonk, NY), was used to compare tumor growth rates between treatment groups. Survival distributions were assessed using Kaplan-Meier plots and the log-rank test. Reaching a tumor volume of 1000 mm^3 or a time period of 54 days post-treatment initiation was each designated as an experimental endpoint. two-way ANOVA analysis in GraphPad Prism Version 8 (San Diego, CA) was used to compare the mean fluorescent intensity levels in imaging experiments, the presence of immune cell populations with the tumors, and mean pixel densities of Proteome Profiler array results for cytokine assessments. Multiple comparisons across treatment groups, as well as across separate time points for the same treatment group, were also determined via 2-way ANOVA. The two-tailed *t* test was used to compare tumor weights. All p values of ≤ 0.05 were considered to indicate statistical significance.

3. Results

3.1. Optimized ratios of alginate and $CaCl_2$ generated uniform, stable nanoparticles

Various nanoparticle formulations were generated and analyzed to define the optimum ratios of alginate-to-$CaCl_2$, alginate-to-protein, alginate-to-protamine sulfate, and the optimal percentage of Pluronic F127. In early formulation studies, cytochrome c was used due to its relatively low cost and to its almost identical molecular weight (CCL21 12.3 kD vs. cytochrome c 12.4 kD) and very similar isoelectric point (CCL21 10.13 versus cytochrome c 10.10) in comparison to CCL21. Pluronic F127 was not incorporated in these early formulations. Since the ratio of sodium alginate to $CaCl_2$ in a nanoformulation could influence particle size and dispersity, nanoparticles with varied mass ratios of alginate to $CaCl_2$ [NaAlg : $CaCl_2$] from 2 to 20) were assessed by DLS to determine the impact of this parameter. At all given ratios, formation of nanoparticles was observed (Fig. S3A). However, particles with monomodal and relatively narrow particle size distribution (PDI < 0.2) were formed in the range of ratios between 4 and 8. Above this ratio, dual and poly-size distributions were detected on DLS, while below this ratio the formation of aggregates was pronounced. Based on these data, we selected the [NaAlg : $CaCl_2$] = 6:1 (w/w) that

corresponds to formation of stable nanoparticles with 180 nm diameter and uniform particle size distribution.

Prior to establishing the final protamine sulfate concentration, alginate to protamine sulfate ratios [NaAlg : PSU] over a range from 20:1 to 2:1 (w/w) were analyzed for use in the nanoformulation. Optimization of protamine sulfate was done at a constant concentration of $CaCl_2$, added for gelation. The size of the particles was practically unchanged in the [NaAlg : PSU] range from 12.5 to 8. Using a higher concentration of protamine sulfate in the reaction mixture led to particles aggregation, while at [NaAlg : PSU] > 12.5 the amount of protamine sulfate was not sufficient to form stable nanoparticles dispersions. Thus, the ratio [NaAlg : PSU] = 10 was set for the alginate nanoparticle formulation. This ratio appeared optimal for achieving unimodal distribution and minimizing alginate nanoparticle size (Fig. S3B). In preliminary experiments, Pluronic F127 was tested over a range of 0.1% to 1.0% in the alginate nanoformulation process. We determined that the concentration of 1% Pluronic F127 resulted in stable nanoparticles with low PDI and small diameter (Fig. S3C).

To investigate protein release rates from our alginate nanoparticles, we tested 4 formulations, which consisted of different alginate : cytochrome c ratios (60:1 w/w versus 6:1 w/w) with or without 1% w/w Pluronic F127, in a dialysis assay at 37°C, pH 7.4 for a prolonged period of time (up to 15 days), which enabled us to simulate CCL21 secretion *in vitro* (Fig. 2A). The amount of cytochrome c released at each time point was then determined by spectrophotometric analysis. Faster release of cytochrome c was exhibited by formulations lacking Pluronic F127 when comparing the same protein : alginate ratios (i.e. cyt. C. (60:1) vs cyt. C. (60:1) + F127, as indicated in Fig. 2A). The (60:1) alginate : cytochrome c formulation without Pluronic F127 had the fastest release rate, followed by the (60:1) alginate : cytochrome c formulation with Pluronic F127. The addition of Pluronic F127 prolonged the release of cytochrome c from the nanoparticles, as indicated by the decreased amount of released cytochrome c across all time points tested when comparing similar protein : alginate ratios. The (6:1) alginate : cytochrome c formulation without Pluronic F127 released cytochrome c at an even more delayed rate, while the (6:1) alginate : cytochrome c formulation with Pluronic F127 released cytochrome c yet more slowly. Overall, the cytochrome c (6:1) + F127 nanoformulation had the slowest rate of release across all 4 formulations tested. The release results for the cytochrome c (6:1) + F127 nanoformulation obtained with the dialysis assay were also confirmed by the incubation method (Fig. 2B).

In addition to assessing the rate of release at the varied alginate : cytochrome c ratios and in the presence versus absence of Pluronic F127, we also analyzed the influence of these parameters on the encapsulation efficiency and loading capacity of the nanoparticles. At a (60:1) alginate : cytochrome c ratio, in the presence versus absence of Pluronic F127, the encapsulation efficiency and loading capacity were 56.0% and 1.5% (respectively) versus 44.0% and 1.1%. At a (6:1) alginate : cytochrome c ratio, in the presence versus absence of Pluronic F127, the encapsulation efficiency and loading capacity were 99.2% and 17.7% (respectively) versus 87.2% and 18.0% (Table S1). Thus, with the (6:1) alginate : cytochrome c ratio, in the presence versus absence of Pluronic F127, the encapsulation

efficiency was much improved. In the presence of Pluronic F127, the encapsulation efficiency was particularly high (99.2%). For the remainder of the experiments described in this report, all nanoformulations were prepared with Pluronic F127 (at 1% w/w), alginate : $CaCl_2$ at a ratio of 6:1, alginate: protamine sulfate ratio of 10:1, and an alginate : protein ratio of 6:1, since this was the best overall combination for prolonged release, excellent encapsulation efficiency, and optimal loading capacity.

3.2. Alginate nanoparticles have high encapsulation efficiency and sustained release of CCL21 in vitro

ELISA was used to assess the efficiency of CCL21 loading. After encapsulation, alginate nanoparticles bearing CCL21 were ultracentrifuged and the supernatant from the centrifugation was collected and analyzed by ELISA (in comparison to a CCL21 standard curve made with known concentrations). Only trace amounts of CCL21 (<1%) were detected in the supernatant, indicating that the efficiency of loading was very high (~99%).

For CCL21-loaded alginate nanoparticles, we determined the release rate by dialysis assay at physiological temperature (37°C) followed by ELISA. The percentage of CCL21 released was calculated using the line of equations generated by the CCL21 standards. As expected, a similar cumulative, prolonged release of CCL21 was observed upon 37°C incubation of the corresponding alginate : CCL21 nanoparticle formulation (containing Pluronic F127) as seen in our previous findings using the (6:1) alginate : cytochrome c nanoparticles that included Pluronic F127 (Fig. 3).

3.3. The spherical alginate nanoparticles have a unimodal size distribution and neutral charge

Our analysis of optimized formulations by DLS revealed that the empty and protein-loaded alginate nanoparticles were < 200 nm in size and had neutral zeta-potential (pH 7.4). Representative values for the sizes of the empty and protein-loaded nanoparticles are shown in Table 1. The empty alginate nanoparticles had a hydrodynamic diameter of 176 ± 5 nm with a PDI value of 0.18, which was the largest of the formulations tested. The cytochrome c-loaded alginate nanoparticles had a diameter of 164 ± 1 nm with a PDI value of 0.11, and the alginate nanoparticles loaded with CCL21 measured 158 ± 3 nm in diameter and had a PDI value of 0.16. Uniform distribution and similarities in size were confirmed by Nanoparticle Tracking Analysis (Table 1). Furthermore, the protein-loaded nanoparticles remained stable in dispersions; no changes in size or PDI were detected for at least 2 months upon storage at 4°C (Fig. S3D).

Visualization of alginate nanoparticles, in both empty and loaded states, was accomplished using AFM and TEM. A representative AFM image of nanoparticles containing CCL21 is shown in Fig. 4A, and similar AFM results for nanoparticles loaded with cytochrome c and for empty nanoparticles are in Fig. S4. TEM images are also displayed in Fig. 4 and Fig. S4, including both empty nanoparticles (Fig. 4B) and nanoparticles bearing CCL21 (Fig. 4C). The images demonstrate that both the empty and CCL21-loaded nanoparticles were well dispersed and had relatively uniform diameters of ~50 nm by TEM and 163 nm by cryo-TEM (Table 1). (It is important to note that in air imaging typically results in decreased

dimensions due to the drying process.) Taken together, the image analysis demonstrated that the nanoparticles were round in shape, had narrow size distributions, and formed little to no aggregates across all 3 formulations.

3.4. Nanoformulated CCL21 significantly inhibited tumor growth and increased the duration of survival compared to CCL21 alone or other controls

We examined the therapeutic efficacy of intratumoral injection of the alginate nanoformulated CCL21 on neuroblastoma tumor growth in a mouse model in 3 separate experiments, which each included 4 treatment groups: nanoformulated CCL21-treated mice ($n = 21$), CCL21-treated mice ($n = 20$), empty nanoparticle-treated mice ($n = 12$), or buffer control-treated mice ($n = 12$). In our studies, the survival endpoint was defined as a tumor volume of 1000 mm^3 or day 54 post-treatment initiation. As described in detail below, the 3 replications yielded consistent results in agent tolerability, tumor growth rates, and modulations in survival, thus validating our experimental strategy and the therapeutic efficacy of the CCL21 nanoformulation. As shown in Fig. 5A, nanoformulated CCL21-treated mice had a significantly ($p < 0.001$) slower tumor growth rate (6.5 mm^3 average increase/day) compared to mice that received buffer control (72.0 mm^3 average increase/day), empty nanoparticles (80.3 mm^3 average increase/day), or CCL21 alone (73.8 mm^3 average increase/day). Importantly, in 33% of the nanoformulated CCL21-treated mice, the palpable tumors completely regressed, in contrast to the mice treated with buffer, nanoparticles alone, or CCL21 alone (Fig. 5). Treatment with nanoformulated CCL21 did not cause significant changes in mouse weight over time (as shown in Fig. S5A up to day 8 post-treatment initiation, which was the time that the first mouse reached the tumor volume endpoint and was euthanized). The tumors were removed from all the mice at the time of necropsy and weighed (with regressed tumors counted as weighing 0 g) (Fig. S5B).

Fig. 6 depicts the survival distributions of all 4 treatment groups. Nanoformulated CCL21 significantly prolonged survival in tumor-bearing mice, compared to those treated with buffer control ($p = 0.008$), empty nanoparticles ($p = 0.002$), or CCL21 only ($p = 0.003$). Mice treated with nanoformulated CCL21 had a mean survival time (i.e., average duration of survival post-treatment initiation) of 26 ± 4.2 days, which was significantly longer than the mean survival of mice that received buffer control (11 ± 0.8 days), empty nanoparticles (11 ± 1.2 days), or CCL21 alone (12 ± 1.3 days).

3.5. Nanoformulated CCL21, as an intratumoral therapy, induced a protective response in a subset of the treated mice

To determine whether an immune response was induced in the mice that had experienced complete tumor regression, we rechallenged all the nanoformulated CCL21-treated mice that had undergone complete tumor regression by subcutaneous injection of Neuro2a neuroblastoma cells into the lower left flank (opposite to the original injection site of Neuro2a cells) on day 54 post-treatment. In parallel, treatment-naïve control mice were subcutaneously injected with Neuro2a cells in the lower left flank. The mice were then monitored daily for the emergence and growth of palpable tumors (tumor volume ≥50 mm^3; Fig. 7). All other treatment groups (buffer control, empty nanoparticles, and free CCL21) failed to induce complete tumor clearance following the initial treatment cycle, and therefore

there were no mice from those other groups that could be included in the rechallenge studies.

The mice that were formerly nanoformulated CCL21-treated and that had showed complete tumor regression remained tumor free upon rechallenge by subcutaneous tumor cell injection of Neuro2A cells (Fig. 7). In contrast, the tumor cell-injected, treatment-naïve control group developed palpable, steadily growing tumors at approximately 8 days post-injection with Neuro2a cells ($p = 0.05$; Fig. 7). Furthermore, the mice in which the tumors had completely regressed had no detectable metastatic disease following rechallenge (as demonstrated by necropsy at day 70 post treatment). These results suggest that nanoformulated CCL21, when administered as an intratumoral therapy, is capable of inducing durable, systemic antitumor protection.

3.6. CCL21 presence within the treated neuroblastoma tumor is increased by delivery in the nanoformulation

To determine the level of CCL21 in the tumor following administration via the nanoformulation, CCL21 was fluorescently labeled with IR800 for visualization *in vivo* in the 800 nm channel with the Pearl® Trilogy Small Animal Imaging System. Three groups ($n = 5$ mice/group) were analyzed in this study: buffer control, CCL21 labeled with IR800 (IR800-CCL21), and nanoformulated IR800-CCL21 (Nanoparticles + IR800-CCL21). Prior to testing in the mice, Nanoparticles + IR800-CCL21 were characterized by DLS analysis for determination of the diameter (average $D_{eff} = 169$ nm) and PDI (average PDI = 0.17), confirming unimodal distribution and similar diameter to nanoformulated unlabeled CCL21.

We examined the intratumoral persistence of the injected Nanoparticles + IR800-CCL21 and the IR800-CCL21 (as compared to buffer control), using the same Neuro2a subcutaneous model of neuroblastoma as described above. The strongest fluorescent signal was observed immediately following the treatments with labeled nanoformulated CCL21 (Fig. 8A, Fig. 8B). Since our treatment regimen consists of 4 treatments over a 2-day period, the marginally ($p = 0.0810$) increased retention of Nanoparticles + IR800-CCL21 relative to IR800-CCL21 at the time of initial imaging (day 0, at 4 hours following the last injection) suggests a very early trend toward nanoformulation-induced potentiation of CCL21 intratumoral accumulation. In comparison with mice treated either with IR800-CCL21 or with buffer, the mice treated with the fluorescently labeled, nanoformulated CCL21 (Nanoparticles + IR800-CCL21) exhibited significantly amplified CCL21 presence in comparison to IR800-CCL21 at days 1 and 2 after the cessation of treatment ($p = 0.0005$ at day 1 and 0.0241 at day 2) (Fig. 8B). Prolonged fluorescence, indicating CCL21 presence, was detectable by *in vivo* imaging for at least 120 hours for both the Nanoparticles + IR800-CCL21-treated mice and the IR800-CCL21-treated mice.

After monitoring the fluorescence intensity over time for all of the mice, at 120 hours we performed necropsies to determine which organs were being utilized for clearance of the nanoparticle components. As shown in Fig. 8C and Fig. 8D, the kidneys exhibited more fluorescence than the liver, spleen, or draining lymph nodes, and thus appear to be functioning as the main clearance organ for the labeled CCL21 (for both the Nanoparticles + IR800-CCL21-treated mice and the IR800-CCL21-treated mice). Notably, at 120 hours, the

tumors of Nanoparticles + IR800-CCL21-treated mice had significantly more fluorescence versus the kidneys ($p = 0.0009$ for kidney 1 and $p = 0.0020$ for kidney 2), indicating that a greater proportion of the CCL21 was still held in the tumor rather than cleared. In contrast, the tumors of the IR800-CCL21-treated mice were not significantly more fluorescent than the kidneys ($p = 0.5592$ for kidney 1 and 0.5344 for kidney 2) at 120 hours.

3.7. The frequencies of total leukocytes, NK cells, and NKT cells were significantly elevated both in tumors treated with nanoformulated CCL21 and with CCL21 alone, but at day 3 the NK cells were significantly increased by nanoformulated CCL21 and not by CCL21 alone

To investigate the fluctuations of immune cell populations within treated neuroblastoma tumors, as a step toward understanding why nanoformulated CCL21 had better therapeutic efficacy than CCL21 alone, we again utilized the neuroblastoma mouse model and treatment strategy described above and compared nanoformulated CCL21, CCL21 alone, or buffer control ($n = 5–10$ mice per group) at days 2, 3, and 7 post treatment initiation. Flow cytometry analysis using antibody panels (Fig. S2, Table S2) allowed for immunophenotypic profiling based on surface marker expression on infiltrating immune cells within the tumor.

The frequency of leukocytes (identified by the CD45 marker) was significantly higher ($p < 0.0001$) at day 2 post-treatment initiation in both the nanoformulated CCL21 and CCL21-alone treatment groups in comparison to tumors treated with buffer control (Fig. 9). Analysis of the $CD45^+$ cell population frequencies at day 3 post-treatment initiation also revealed significantly increased percentages of $CD45^+$ cells in the nanoformulated CCL21 treatment group ($p = 0.019$) and in the CCL21 treatment group ($p = 0.009$) versus the control group. At day 7, similar percentages of $CD45^+$ cell frequencies were observed in all groups.

NK and NKT cell populations demonstrated increased frequencies in nanoformulated CCL21 and CCL21-treated groups (compared to buffer control) over time (Fig. 10). The nanoformulated CCL21 and CCL21 treatments resulted in a significantly higher frequency of NK cells within the tumor at day 2 ($p = 0.0168$ and $p = 0.0169$, respectively). The nanoformulated CCL21-treated tumors, but not the CCL21 alone-treated tumors, also exhibited a significantly ($p = 0.0138$) higher percentage of NK cells within the tumor at day 3 compared to those treated with buffer control, indicating a difference in the effects of the 2 treatments at day 3. The percent of NKT cells at day 2 was significantly higher in both treatment groups ($p = 0.0039$ and $p = 0.0029$, respectively) compared to the control. Comparisons within treatment groups show significant decreases in the percentages of NK and NKT cells within tumors treated with either nanoformulated CCL21 or CCL21 alone over time, whereas buffer control-treated tumors remained relatively low throughout the study (Fig. 10).

3.8. Tumors treated either with nanoformulated CCL21 or CCL21 alone demonstrated a significant increase in DC frequency, as well as macrophage frequency and phagocytic marker expression

The percentage of DCs was significantly lower in the buffer control group on day 2 in comparison to the nanoformulated CCL21 group ($p = 0.0081$) and the CCL21 group ($p =$

0.0259) (Fig. S6). Thus, in the tumors of both nanoformulated CCL21-treated and CCL21-treated mice, there was a significant increase in the frequency of DCs, as well as in the DCs expressing higher levels of CD80 and CD86, indicating activation (Fig. S6C). In our study, we found that macrophage frequencies within tumors were significantly higher for nanoformulated CCL21 ($p = 0.0007$) and for CCL21-alone ($p = 0.0038$) treatment groups than for the buffer control group at day 2 post-treatment initiation (Fig. S7). Furthermore, comparing macrophage frequencies within each treatment group over time shows nanoformulated CCL21 and CCL21-alone treatment resulted in significant ($p < 0.01$) stepwise decreases over time (Fig. S7A). Mer, as a marker of increased macrophage phagocytic activity, was analyzed and the data for this marker are shown in Fig. S7B and Fig. S7C. The frequency of Mer-expressing macrophages was significantly elevated at day 2 post-treatment in the nanoformulated CCL21-treated tumors ($p = 0.0131$) and in CCL21-treated tumors ($p = 0.0047$) versus the control group. Analysis of the median fluorescent intensity (MFI) of Mer showed that a robust ($p < 0.03$) increase in MFI occurred on day 3 post-treatment in the groups treated with either CCL21 modality compared to the control. Differentiating the $F4/80^+$ macrophage population into either M1 ($CD38^+$) or MDSC ($Gr\text{-}1^+$) revealed that only the nanoformulated CCL21 treatment, and not the free CCL21 treatment, was able to induce a trend toward a rise in the frequency of M1 macrophages within the tumor at day 3 (Fig. S7D). MDSC-type macrophages trended higher at day 2 for both the nanoformulated CCL21-treated tumors and CCL21-treated tumors, compared to buffer control (Fig. S7E).

3.9. Both nanoformulated CCL21-treated and free CCL21-treated tumors showed an increase in the frequency of $CD4^+$ and $CD8^+$ T cells, but not memory B cells

As shown in Fig. S8A, at day 2 post-treatment initiation there was a significantly higher percentage of $CD4^+$ T cells in tumors treated with nanoformulated CCL21 ($p = 0.0105$) or CCL21 alone ($p = 0.0178$) versus the buffer control. Nanoformulated CCL21-treated tumors, but not free CCL21-treated tumors, at day 3 post-treatment initiation had marginally ($p = 0.0608$) more $CD4^+$ T cells than the buffer control. Additional analysis of $CD4^+$ T cells subpopulations revealed no significant differences among groups or among any group's days post-treatment results for T regulatory cells (Fig. S8B), effector T cells (Fig. S8C), effector memory T cells (Fig. S8D), central memory T cells (Fig. S8E), or naïve T cell populations (Fig. S8F). Effector (Fig. S8C) and effector memory (Fig. S8D) $CD4^+$ T cell populations were either maintained or trended toward an increase over time for all groups. Central memory $CD4^+$ T cell population frequencies were marginally elevated at days 2 and 7 in the nanoformulated CCL21-treated and CCL21-treated groups ($p = 0.0665$ and $p = 0.0659$, respectively) compared to tumors treated with the buffer control (Fig. S8E).

$CD8^+$ T cell populations were significantly increased in tumors treated with nanoformulated CCL21 ($p = 0.007$) or CCL21 ($p = 0.041$) when compared to the control at day 2 post-treatment (Fig. S9A). Marginal increases in the percentage of $CD8^+$ T cell populations at day 3 post treatment initiation were also seen in nanoformulated CCL21-treated and CCL21 alone-treated tumors versus the control ($p = 0.0837$ and $p = 0.0739$, respectively). Effector and effector memory $CD8^+$ T cell population frequencies were found to trend higher or be maintained over time in all of the treatment groups (Fig. S9B and Fig. S9C). Trends toward

higher frequencies in $CD8^+$ central memory and naïve T cell populations were observed with the nanoformulated CCL21 and CCL21 treatment groups compared to the control (Fig. S9D).

In addition to the assessment of T cell infiltration, the frequency of memory B cells within the tumors was also examined. Relative to the buffer control, memory B cell frequency was not significantly elevated in tumors treated with either nanoformulated CCL21 or CCL21 alone following treatment (Fig. S10). A trend toward higher memory B cell infiltration was observed at day 3 post-treatment in all treatment groups (Fig. S10).

3.10. Immune cell infiltrates of mice with regressing tumors exhibited specific characteristics

As was the case in the abovementioned experiment focused on monitoring tumor volume and survival, in our experiment to analyze intratumoral immune infiltration there were some mice treated with nanoformulated CCL21 (but not CCL21 alone or buffer) whose tumors underwent regression. The frequencies of various types of immune cells in the tumors that regressed, and in the tumor of an additional mouse that began to slightly regress but quickly regrew to its original size are highlighted in circles with separate colors (Fig. 11A). (In the graph shown in Fig. 11, if a colored circle is hidden behind another circle, an arrow of the same color is used to indicate the position of that circle.) The immune cell types included in the graph are NK cells (Fig. 11B), NKT cells (Fig. 11C), DCs (Fig. 11D), $CD4^+$ T cells (Fig. 11E), $CD8^+$ T cells (Fig. 11F), macrophages (Fig. 11G), M1 macrophages (Fig. 11H), and MDSC macrophages (Fig. 11I). Two of the mice (Mouse 1 and Mouse 2) were already exhibiting regression by day 3 post-treatment initiation (which was their experimental endpoint for euthanasia and tumor harvest). Mouse 1 (indicated as a red dot) demonstrated a 23% decrease in tumor volume following treatment initiation, and the tumor exhibited high frequencies of innate immune cells, particularly DCs ($CD45^+$ cells: 35.5 %, NK cells: 2.98%, NKT cells: 5.81%, DCs: 29.5%, $CD4^+$ T cells: 0.33%, $CD8^+$ T cells: 0.38%, macrophages: 14.5%, M1 macrophages: 4.07%, MDSC macrophages 2.89%). Similarly, Mouse 2 (indicated in blue) had an 18% decrease in tumor volume following treatment initiation, and at day 3 innate immune cell populations (predominantly DCs) were plentiful within the tumor ($CD45^+$ cells: 34.2%, NK cells: 3.03 %, NKT cells: 4.26%, DCs: 25.2%, $CD4^+$ T cells: 0.28%, $CD8^+$ T cells: 0.30%, macrophages: 11.2%, M1 macrophages: 1.34%, MDSC macrophages 2.11%). In contrast, Mouse 3 (indicated in purple) had a slowly growing tumor that fluctuated between growth and regression, and at day 7 post-treatment initiation (the experimental endpoint for this mouse), the tumor volume was almost identical to the initial tumor volume. Mouse 3's tumor had relatively few innate immune cells, with low levels of DCs and an increased MDSC/M1 ratio ($CD45^+$ cells: 4.83%, NK cells: 0.20%, NKT cells: 0.031%, DCs: 0.73%, $CD4^+$ T cells: 0.19%, $CD8^+$ T cells: 0.11%, macrophages: 2.60%, M1 macrophages: 0.49%, and MDSC macrophages: 1.29%). Mouse 4 (indicated in green) had a tumor that increased in volume from day 0 to day 2 but then steadily declined (19.5% decrease) from day 2 to day 7 post treatment initiation, at which time its tumor was found to have higher innate immune cell frequencies than Mouse 3 and also slight elevations in T cell frequencies ($CD45^+$ cells: 17.7 %, NK cells: 1.080%, NKT cells: 0.120%, DCs:

6.69%, $CD4^+$ T cells: 2.21%, $CD8^+$ T cells: 1.11%, macrophages: 5.26%, M1 macrophages: 0.97%, and MDSC macrophages: 1.81%).

3.11. In general, nanoformulated CCL21-treated tumors had higher, more prolonged levels of anti-tumor cytokines and decreased levels of pro-tumor cytokines

A multiplex approach was used to investigate the cytokine profiles of treated neuroblastoma tumors derived from the same mice that were used for the aforementioned immune cell infiltration experiments at days 2 and 7 post-treatment initiation. Treatment with either nanoformulated CCL21 or free CCL21 resulted in varied changes in the level of cytokines present within the samples derived from mice at day 2 and day 7 post-treatment initiation (Fig. 12, Fig. 13, and Fig. S11). The multiplex analysis revealed treatment-dependent changes in anti-tumor cytokines (CXCL9, CXCL10, IFN-γ, IL-12p70, CCL3, and CCL2) (Fig. 12) as well as in pro-tumor cytokines (IL6, TIMP-1 and IL-16) (Fig. 13).

Overall, nanoformulated CCL21 was best able to successfully induce expression levels of anti-tumor cytokines that were both increased and of longer duration. For example, as displayed in Fig. 12, while a decrease in CXCL9 levels over time was observed across all 3 treatment groups, the nanoformulated CCL21 treatment caused a much more enhanced and persistent presence of CXCL9 within the tumor at both days 2 and 7 post-treatment initiation in comparison with the other treatments ($p < 0.0001$). Furthermore, at day 7, nanoformulated CCL21 treated resulted in significantly higher CXCL10 expression compared to CCL21 ($p = 0.0013$) (Fig. 12). At day 2, the level of IFN-γ in tumors of nanoformulated CCL21-treated mice was approximately 2-fold higher than in tumors of CCL21-treated mice ($p < 0.0001$), although the IFN-γ levels were similar at day 7. Similarly, IL-12 p70 was ~2-fold higher in tumors of nanoformulated CCL21-treated mice at day 2, compared to the level in tumors of CCL21-treated mice ($p < 0.001$), but was not significantly higher than in tumors of CCL21-treated mice at day 7. CCL3 was significantly higher ($p <0.0001$) in samples from CCL21-treated tumors at day 2 post-treatment than in tumors treated with nanoformulated CCL21 (Fig. 12). A steep decline in CCL3 was observed in CCL21-treated tumors at day 7 whereas the nanoformulated CCL21 treatment group showed a marginal increase. Nanoformulated CCL21, but not CCL21, was capable of inducing significantly elevated ($p < 0.0001$) levels of CCL2 that persisted over time (Fig. 12).

In addition to the enhanced antitumor effects exhibited by nanoformulated CCL21, we also found that the level of the pro-tumor cytokine IL-6 remained constant over time and at a level significantly lower in the nanoformulated CCL21-treated tumors ($p < 0.0001$) than in tumors treated with CCL21 (Fig. 13). Nanoformulated CCL21 treatment was also able to decrease the levels of the pro-tumor cytokine IL-16 significantly over time in comparison to CCL21 alone (Fig. 13). In contrast to the positive effect of nanoformulated CCL21 on reducing IL-6 and IL-16 in the tumors, the tumors treated with nanoformulated CCL21 had significantly greater levels of another pro-tumor cytokine, TIMP-1, than those treated with CCL21 (Fig. 13). Both nanoformulated CCL21 treatment and free CCL21 treatment resulted in proportional declines in the level of TIMP-1 over time (Fig. 13).

4. Discussion

The immunotherapeutic potential of CCL21, as a cancer treatment, has been previously analyzed using various cancer models and methods of delivery, and investigation of CCL21 therapy for tumors has advanced to clinical trials [1–11,65–66]. CCL21, when administered intratumorally, has been found to result in tumor growth inhibition, infiltration of DCs, $CD4^+$ T cells, and $CD8^+$ T cells, and demonstration of systemic antitumor immunity in models of lung, breast, and pancreatic cancers, melanoma, head and neck cancer, and other cancers, as reported in our studies and those by other laboratories [1–5,9–11]. Several modes of delivering CCL21 have been tested with the objective of further increasing CCL21's therapeutic impact [5,8–11, 65–68]. While these modes of CCL21 delivery have shown potential, they have varied degrees of limitations concerning the logistics of production and administration, loading capacity, duration of therapeutic effect, injectability, and/or cost, thus presenting a need for enhanced systems of delivery for CCL21 that are easily produced, biocompatible, and injectable.

Applications of nanoparticles as drug delivery platforms have dramatically widened over recent years, and nanoparticles have been adopted for numerous medical purposes to provide well-controlled release of therapeutic agents. Many techniques have been developed for nanoparticle fabrication, and among the polymers tested, alginate is one that has been used as a carrier for a variety of biological agents, such as genes, antigens, and various proteins, allowing protection of these therapeutic agents during transit. Alginates have emerged as one of the most extensively explored biomaterials, owing to its excellent biocompatibility, biodegradation, sol-gel transition properties, and chemical versatility. Such characteristics make possible many modifications of alginate to shape the properties of nanoparticles according to specific applications. As described in this current report, we generated novel alginate nanoparticles to deliver CCL21 as an injectable and biocompatible therapeutic nanoformulation for neuroblastoma treatment. Our choice of alginate was based on its excellent safety record, ease of modification for protein cargo delivery, and anionic polysaccharide chains that facilitate its interaction with CCL21 (which has a net cationic charge). For materials such as proteins, avoiding harsh conditions upon handling is crucial, and a natural polysaccharide like alginate is an excellent candidate for encapsulation of CCL21. The nanoparticles were prepared by ionotopic gelation, avoiding high temperatures and organic solvents that could potentially compromise the biological activity of the protein. At the same time, this nanoformulation allowed very high loading and the desired release profile.

The gelation rate and the temperature at which gelation occurs are critical in establishing the mechanical integrity of the nanoparticles [25]. However, temperature, pH, and time are also important for stimulating the proton-catalyzed hydrolysis of alginates within the particle, which leads to the release of the cargo [26]. Therefore, optimization of nanoparticle stability by varying the alginate : $CaCl_2$ ratio (Fig. S3A) and the alginate : protamine sulfate ratio (Fig. S3B) was essential for producing small, uniform nanoparticles. The developed set of the alginate gelation parameters allowed achievement of a loading capacity for CCL21 of about 17%, which is substantially higher compared to reported protein loading in conventional PLGA micro- and nanoparticles and liposomes. Indeed, Giteau et al. used

protein precipitation to ensure stability upon encapsulation into PLGA microspheres and were able to achieve about 0.5% loading with respect to lysozyme [69]. Modification of this methodology resulted in the production of lysozyme or cytochrome c-loaded PLGA nanoparticles with loading capacity close to 5% [70]. The modest protein loading capacity of an order of ~2–3% was also reported for small size liposomes (50–150 nm) and was attributed to a low entrapment volume of liposomes [71]. In the case of the alginate nanoparticles, it is likely that the electrostatic interactions of CCL21 (a weakly cationic protein) with the negatively charged alginate chains and porous structure of the formed gels are beneficial for higher protein loading. An entrapment of relatively high content of protein (at a 6:1 ratio of alginate to protein) did not appear to interfere with network formation. However, the further attempts to increase the loading by decreasing the alginate to protein ratio resulted in precipitation. The *in vitro* release rate was also shown to be governed by the ratio of alginate to protein with unexpectedly slower release observed at relatively high protein loading (Fig. 2A). It is likely that the high protein loading (6:1 ratio) may result in additional physical crosslinking of alginate chains within the gel network compared to nanoparticles with low protein loading (60:1 ratio), which correspondingly might slow down diffusional mobility and following release kinetics of protein. It is also possible that heterogeneities in protein distribution throughout the gel network at higher loading can influence cargo release from the gel matrix. Full elucidation of these complex mechanisms will require more detailed investigation in future studies. The presence of the Pluronic F127 contributes to the stability of the alginate nanoparticle matrix, making it more compact and less leaky, therefore leading to a further decrease in protein release rate. Thus, based on our pilot experiments with cytochrome c, the remainder of our work utilized alginate nanoparticles formulated with CCL21 at a 6:1 ratio of alginate to protein and incorporated Pluronic F127.

Nanoformulated CCL21 treatment of the mouse neuroblastoma tumors resulted in slower tumor growth and longer survival than treatment with CCL21 (Fig. 5 and Fig. 6). A third of the mice treated with nanoformulated CCL21 underwent complete tumor regression (Fig. 5 and Fig. 6). Although only a minority of the nanoformulated CCL21-treated mice experienced complete regression of their tumors, this finding parallels the observations in cancer immunotherapy clinical trials that commonly only a small proportion of patients exhibit positive responses [72]. To gain insight into the *in vivo* mechanisms for nanoformulated CCL21's therapeutic activity, we performed tracking studies and analysis of intratumoral immune cell populations and cytokines. From our tracking of fluorescently labeled CCL21 delivered in nanoparticles, we detected a higher level of fluorescence in the tumors at day 1 and day 2 following treatment, relative to fluorescently labeled free CCL21 administered to the tumors (Fig. 8). In our investigation of immune cell populations in nanoformulated CCL21- versus CCL21-treated tumors, the average frequency of NK cells at day 3 was significantly higher in the tumors of mice that had been injected with nanoformulated CCL21, suggesting a role for NK cells in the therapeutic effects. This theory is further supported by the relatively high frequency of NK cells in the tumors of mice whose tumors were undergoing regression by day 3 (Fig. 11B). Observation of the frequencies of immune cell subsets in these mice whose tumors were regressing by day 3

also reveals increased levels of NKTs (Fig. 11C), DCs (Fig. 11D), and macrophages (even including MDSC macrophages) (Fig. 11G, Fig. 11H, and Fig. 11I).

In our study, assessment of cytokine levels was also very informative, showing heightened levels of CXCL9, CXCL10, IFN-γ, IL-12 p70, CCL3, and CCL2 in the tumors of nanoformulated CCL21-treated mice (as compared to CCL21-treated mice) at day 2 or day 7 (or both) post-treatment (Fig. 12 and Fig. S11). These cytokines have all had anti-tumor effects ascribed to them. The anti-tumor effects of CXCL9, CXCL10, and IFN-γ have been reported for many cancer types, including serous ovarian and colorectal cancers [73–74]. CCL3-stimulated, IFN-γ-mediated recruitment of NK and $CD103^+$ DCs was demonstrated to enhance tumor rejection and $CD8^+$ T cell infiltration in a colon cancer model [75]. Previous studies have shown that the efficacy of CCL21 therapy in lung and breast cancers is linked to CXCL9, CXCL10, and/or IFN-γ. This trio of cytokines enhances immune reactivity against tumors, in coordination with additional cytokines [76–79]. Our finding of elevated levels of IL-12 p70 in nanoformulated CCL21-treated tumors (Fig. 12) corresponds with the previously reported anti-tumor effects of IL-12 in neuroblastoma [80–81]. In addition, CCL3, in conjunction with IFN-γ, is capable of augmenting anti-tumor immune priming in the lymph node in a manner that is NK cell dependent [82]. In addition to up-regulating the presence of anti-tumor cytokines, nanoformulated CCL21 also down-regulated the expression of pro-tumor IL-6 and IL-16 in the tumor (Fig. 13). IL-6 is specifically recognized for promoting neuroblastoma growth [83–84]. However, unexpectedly, nanoformulated CCL21 also increased the presence of TIMP-1 (Fig. 13), which has been reported to have pro-tumor effects in the neuroblastoma setting [85].

In patients, intratumoral injection of neuroblastoma tumors with nanoformulated CCL21 would be feasible, since internal anatomical sites at which neuroblastoma tumors can be present are identifiable and accessible in patients by the use of available imaging techniques. Most children at relapse have ^{131}I- or ^{123}I-meta-iodobenzylguanidine scintiscan results that would identify a number of lesions that would be amenable to nanoformulated CCL21 injection, and these CCL21 nanoparticles are sufficently small for delivery to internal organs. Neuroblastoma tumors can also be present near the skin's surface on patients, where they present at palpable lesions. High-risk neuroblastoma patients often have readily palpable tumor metastases that would be very easily treatable by injection of nanoformulated CCL21 in the clinical setting. Since the activity of nanoformulated CCL21 spurs a systemic immune response, rather than only a local one, it would only need to be administered to a single metastasis, not to multiple sites. With other types of systemically effective immunotherapy, reduction even in bone metastases has been demonstrated [86–87], which supports the feasibility of nanoformulated CCL21's systemic immune influence being effective against neuroblastoma bone metastases as well as against soft tissue metastases.

5. Conclusion

In conclusion, we have designed an injectable, slow-release alginate-based nanoformulation of CCL21 that has shown promise as an immunotherapeutic modality for neuroblastoma treatment in our studies. A great benefit of nanoformulated CCL21 intratumoral therapy is that it provides personalized immunotherapy by using the tumor itself as the "vaccine,"

while only requiring a single, non-personalized type of treatment (i.e., the nanoformulated CCL21). In addition to nanoformulated CCL21's usefulness in neuroblastoma treatment, potentially other cancers for which CCL21 has previously been shown to be effective may benefit even more from treatment with this alginate nanoformulation of CCL21 than from treatment with CCL21 alone. In addition, alginate nanoparticle versatility provides additional avenues, including the use of multiple cargoes, which are options that we plan to pursue in the future. Taken together, our findings support further development and characterization of nanoformulated CCL21 as an intratumoral immunotherapy for cancer.

Supplementary Material

Refer to Web version on PubMed Central for supplementary material.

Acknowledgments

Funding from the UNMC Pediatric Cancer Research Center and the UNMC Fred & Pamela Buffett Cancer Center Support Grant (National Cancer Institute P30CA036727) is acknowledged. Support was also provided by UNMC Graduate Studies Fellowships (to B.P. and B.S.) and by the Cancer Biology Training Grant (National Cancer Institute T32CA009476). We also acknowledge the technical support of the Nanomaterials Core Facility of the Center for Biomedical Research Excellence (CoBRE) Nebraska Center for Nanomedicine (supported by an Institutional Development Award from the National Institute of General Medical Sciences under grant number P30GM127200). The authors would like to thank Dr. Alexander Lushnikov and Dr. Alexey Krasnoslobodtsev for technical assistance with AFM imaging at the UNMC Nanoimaging Core Facility, which is partly supported by funds from the Nebraska Research Initiative (NRI). The authors also thank Tom Bargar and Nicholas Conoan of the UNMC Electron Microscopy Core Facility (EMCF) for technical assistance. The EMCF is supported by state funds from the NRI and the University of Nebraska Foundation, and institutionally by the UNMC Office of the Vice Chancellor for Research. Technical assistance for this study was also provided by the staff of the UNMC Comparative Medicine Facility and the UNMC Flow Cytometry Research Facility. The UNMC Flow Cytometry Research Facility is administrated through the Office of the Vice Chancellor for Research and supported by state funds from the NRI and the Fred & Pamela Buffett Cancer Center's National Cancer Institute Cancer Center Support Grant (P30CA036727). Major instrumentation for the Flow Cytometry Research Facility has been provided by the Office of the Vice Chancellor for Research, the University of Nebraska Foundation, the Nebraska Banker's Fund and by the NIH-NCRR Shared Instrument Program. The funding sources for this project had no involvement in the study design, in the collection, analysis, and interpretation of the data, in the writing of the manuscript, or in the decision to submit the manuscript for publication.

References

[1]. Turnquist HR, Lin X, Ashour A, Hollingsworth MA, Singh RK, Talmadge JE, Solheim JC, CCL21 induces extensive intratumoral immune cell infiltration and specific anti-tumor cellular immunity. Int. J. Oncol 30 (2007) 631–639. [PubMed: 17273764]

[2]. Ashour AE, Lin X, Wang X, Turnquist HR, Burns NM, Tuli A, Sadanandam A, Suleiman K, Singh RK, Talmadge JE, Solheim JC, CCL21 is an effective surgical neoadjuvant for treatment of mammary tumors. Cancer Biol. Ther 6 (2007) 1206–1210. [PubMed: 17617742]

[3]. Sharma S, Stolina M, Zhu LX, Lin Y, Batra R, Huang M, Strieter R, Dubinett SM, Secondary lymphoid tissue chemokine reduces pulmonary tumor burden in spontaneous murine bronchoalveolar cell carcinoma. Cancer Res 61 (2001) 6406–6412. [PubMed: 11522634]

[4]. Kirk CJ, Hartigan-O'Connor D, Mulé JJ, The dynamics of the T-cell antitumor response: chemokine-secreting dendritic cells can prime tumor-reactive T cells extranodally. Cancer Res. 61 (2001) 8794–8802. [PubMed: 11751401]

[5]. Dubinett SM, Lee JM, Sharma S, Mulé JJ, Chemokines: can effector cells be redirected to the site of the tumor? Cancer J 16 (2010) 325–335. [PubMed: 20693843]

[6]. Liang CM, Zhong CP, Sun RX, Liu BB, Huang C, Qin J, Zhou S, Shan J, Liu YK, Ye SL, Local expression of secondary lymphoid tissue chemokine delivered by adeno-associated virus within the tumor bed stimulates strong anti-liver tumor immunity. J. Virol 81 (2007) 9502–9511. [PubMed: 17567706]

[7]. Yousefieh N, Hahto SM, Stephens AL, Stephens AL, Ciavarra RP, Regulated expression of ccl21 in the prostate microenvironment inhibits tumor growth and metastasis in an orthotopic model of prostate cancer. Cancer Microenviron 2 (2009) 59–67. [PubMed: 19418243]

[8]. Kar UK, Srivastava MK, Andersson A, Baratelli F, Huang M, Kickhoefer VA, Dubinett SM, Rome LH, Sharma S, Novel CCL21-vault nanocapsule intratumoral delivery inhibits lung cancer growth. PLoS One 6 (2011) e18758. [PubMed: 21559281]

[9]. Hu D, Lau OD, Wang L, Wang G, Schaue D, Zhu L, Huang M, Lin Y, Dennis M, Abemayor E, Elashoff DA, Dubinett SM, McBride WH, Sharma S, Wu B, St John MA, A novel modular polymer platform for the treatment of head and neck squamous cell carcinoma (HNSCC) in an animal model. Arch. Otolaryngol Head Neck. Surg 138 (2012) 412–417. [PubMed: 22508626]

[10]. Lin Y, Luo J, Suwarnasar A, Zhu WE, Zhu L, Srivastava M, Schaue D, McBride W, Abemayor E, Elashoff DA, Dubinett SM, Sharma S, Wu B, St John MA, A polymer that delivers cytokines and cisplatin is effective in reducing tumor burden in HNSCC. Otolaryngol. Head Neck Surg 151 (2014) 447–453. [PubMed: 24825873]

[11]. Pellionisz PA, Lin Y, Mallen-St Clair J, Luo J, Suwarnasarn A, Schaue D, Elashoff DA, Palma-Diaz F, Dubinett SM, Sharma S, Wu B, St John MA, Use of a novel polymer in an animal model of head and neck squamous cell carcinoma. Otolaryngol. Head Neck Surg 158 (2018) 110–117. [PubMed: 28895464]

[12]. Messina JL, Fenstermacher DA, Eschrich S, Qu X, Berglund AE, Lloyd MC, Schell MJ, Sondak VK, Weber JS, Mulé JJ, 12-chemokine gene signature identifies lymph node-like structures in melanoma: potential for patient selection for immunotherapy? Sci Rep 2 (2012) 765. [PubMed: 23097687]

[13]. Gunn MD, Tangemann K, Tam C, Cyster JG, Rosen SD, Williams LT, A chemokine expressed in lymphoid high endothelial venules promotes the adhesion and chemotaxis of naïve T lymphocytes. Proc. Natl. Acad. Sci. USA 95 (1998) 258–263. [PubMed: 9419363]

[14]. Willimann K, Legler DF, Loetscher M, Roos RS, Delgado MB, Clark-Lewis I, Baggiolini M, Moser B. The chemokine SLC is expressed in T cell areas of lymph nodes and mucosal lymphoid tissues and attracts activated T cells via CCR7. Eur. J. Immunol 28 (1998) 2025–2031. [PubMed: 9645384]

[15]. Cyster JG. Chemokines and cell migration in secondary lymphoid organs. Science. 286 (1999) 2098–2102. [PubMed: 10617422]

[16]. Cooper MA, Fehniger TA, Caligiuri MA. The biology of human natural killer-cell subsets. Trends Immunol 22 (2001) 633–640. [PubMed: 11698225]

[17]. Robertson MJ. Role of chemokines in the biology of natural killer cells. J. Leukoc. Biol. 7 (2002) 173–183.

[18]. Wu S, Xing W, Peng J, Yuan X, Zhao X, Lei P, Li W, Wang M, Zhu H, Huang B, Huang L, Shen G, Tumor transfected with CCL21 enhanced reactivity and apoptosis resistance of human monocyte-derived dendritic cells. Immunobiology 213 (2008) 417–426. [PubMed: 18472050]

[19]. Yanagawa Y, Onoé K, CCR7 ligands induce rapid endocytosis in mature dendritic cells with concomitant up-regulation of Cdc42 and Rac activities. Blood 101 (2003) 4923–4929. [PubMed: 12609829]

[20]. Thanarajasingam U, Sanz L, Diaz R, Qiao J, Sanchez-Perez L, Kottke T, Thompson J, Chester J, Vile RG, Delivery of CCL21 to metastatic disease improves the efficacy of adoptive T-cell therapy. Cancer Res 67 (2007) 300–308. [PubMed: 17210711]

[21]. Selvakumaran M, Pisarcik DA, Bao R, Yeung AT, Hamilton TC, Enhanced cisplatin cytotoxicity by disturbing the nucleotide excision repair pathway in ovarian cancer cell lines. Cancer Res 63 (2003) 1211–1216.

[22]. Chen P, Luo S, Wen YJ, Li YH, Li J, Wang YS, Du LC, Zhang P, Tang J, Yang DB, Hu HZ, Zhao X, Wei YQ, Low-dose paclitaxel improves the therapeutic efficacy of recombinant adenovirus encoding CCL21 chemokine against murine cancer. Cancer Sci 105 (2014) 1393–1401. [PubMed: 25230206]

[23]. Christian DA, Hunter CA, Particle-mediated delivery of cytokines for immunotherapy. Immunotherapy 4 (2012) 425–441. [PubMed: 22512636]

[24]. Lee KY, Mooney DJ, Alginate: properties and biomedical applications. Progress in Polymer Sci 37 (2012) 106–126.

[25]. Kuo CK, Ma PX, Ionically crosslinked alginate hydrogels as scaffolds for tissue engineering: part 1. Structure, gelation rate, and mechanical properties. Biomaterials 22 (2001) 511–521. [PubMed: 11219714]

[26]. Tonnesen HH, Karlsen J, Alginate in drug delivery systems. Drug Dev. Ind. Pharm 28 (2002) 621–630. [PubMed: 12149954]

[27]. Gombotz WR, Wee SF, Protein release from alginate matrices. Adv. Drug Delivery Rev 31 (1998) 267–285.

[28]. Wang Y, Irvine DJ, Engineering chemoattractant gradients using chemokine-releasing polysaccharide microspheres. Biomaterials 32 (2011) 4903–4913. [PubMed: 21463892]

[29]. Siegel RL, Miller KD, Jernal A, Cancer statistics, 2020. CA Cancer J. Clin 70 (2020) 7–30. [PubMed: 31912902]

[30]. Brodeur GM, Neuroblastoma: biological insights into a clinical enigma. Nat. Rev. Cancer 3 (2003) 203–216. [PubMed: 12612655]

[31]. Maris JM, Recent advances in neuroblastoma. N. Engl. J. Med 362 (2010) 2202–2211. [PubMed: 20558371]

[32]. Johnsen JI, Dyberg C, Fransson S, Wickstrom M, Molecular mechanisms and therapeutic targets in neuroblastoma. Pharmacol. Res 131 (2018) 164–176. [PubMed: 29466695]

[33]. Park JR, Eggert A, Caron H, Neuroblastoma: biology, prognosis and treatment. Hematol. Oncol. Clin. North Am 24 (2009) 65–86.

[34]. Monclair T, Brodeur GM, Ambros PF, Brisse HJ, Cecchetto G, Holmes K, Kaneko M, London WB, Matthay KK, Nuchtern JG, von Schweinitz D, Simon T, Cohn SL, Pearson ADJ, The international Neuroblastoma Risk Group (INRG) staging system: an INRG task force report. J. Clin. Oncol 27 (2009) 289–297. [PubMed: 19047291]

[35]. Cohn SL, Pearson ADJ, London WB, Monclair T, Ambros PF, Brodeur GM, Faldum A, Hero B, Iehara T, Machin D, Mosseri V, Simon T, Garaventa A, Castel V, Matthay KK, The International Neuroblastoma Risk Group (INRG) classification system: an INRG task force report. J. Clin. Oncol 27 (2009) 289–297. [PubMed: 19047291]

[36]. Davidoff AM, Neuroblastoma. Semin. Pediatr. Surg 21 (2012) 2–14. [PubMed: 22248965]

[37]. Lau L, Tai D, Weitzman S, Grant R, Baruchel S, Malkin D. Factors influencing survival in children with recurrent neuroblastoma. J. Pediatr. Hematol. Oncol 26 (2004) 227–232. [PubMed: 15087949]

[38]. Li R, Polishchuk A, DuBois S, Hawkins R, Lee SW, Bagatell R, Shusterman S, Hill-Kayser C, Al-Sayegh H, Diller L, Haas-Kogan DA, Matthay KK, London WB, Marcus KJ, Patterns of relapse in high-risk neuroblastoma patients treated with and without total body irradiation. Int. J. of Radiation Oncol. Biol. Phys 97 (2017) 270–277.

[39]. Matthay KK, Villablanca JG, Seeger RC, Stram DO, Harris RE, Ramsay NK, Swift P, Shimada K, Black CT, Brodeur GM, Gerbing RB, and Reynolds PR, Treatment of high-risk neuroblastoma with intensive chemotherapy, radiotherapy, autologous bone marrow transplantation, and 13-*cis*-retinoic acid. N. Engl. J. Med 341 (1999) 1165–1173. [PubMed: 10519894]

[40]. Matthay KK, Reynolds CP, Seeger RC, Shimada H, Adkins ES, Haas-Kogan D, Gerbing RB, London WB, and Villablanca JG, Long-term results for children with high-risk neuroblastoma treated on a randomized trial of myeloablative therapy followed by 12-*cis*-retinoic acid: a Children's Oncology Group study. J. Clin. Oncol 27 (2009) 1007–1013. [PubMed: 19171716]

[41]. London WB, Castel V, Monclair T, Ambros PF, Pearson ADJ, Cohn SL, Berthold F, Nakagawara A, Ladenstein RL, Iehara T, and Matthay KK, Clinical and biological features predictive of survival after relapse of neuroblastoma: a report from the International Neuroblastoma Risk Group Project. J. Clin. Oncol 29 (2011) 3286–3292. [PubMed: 21768459]

[42]. Zage PE, Novel therapies for relapsed and refractory neuroblastoma. Children 5 (2018) 148; doi:10.3390/children5110148

[43]. Oeffinger KC, Merten AC, Sklar CA, Kawashima T, Hudson MM, Meadows AT, Friedman DL, Marina N, Hobbie W, Kadan-Lottick NS, Schwartz CL, Leisenring W, Robison LL, Chronic

health conditions in adult survivors of childhood cancer. N. Engl. J. Med 355 (2006) 1572–1582. [PubMed: 17035650]

[44]. Applebaum MA, Vaksman Z, Mee Lee S, Hungate EA, Henderson TO, London WB, Pinto N, Volchenboum SL, Park JR, Naranjo A, Hero B, Pearson AD, Stranger BE, Cohn SL, Diskin SJ, Neuroblastoma survivors are at increased risk for second malignancies: a report from the International Neuroblastoma Risk Group Project. Eur. J. Cancer 72 (2017) 177–185. [PubMed: 28033528]

[45]. Mertens AC, Yasui Y, Neglia JP, Potter JD, Nesbit ME, Ruccione K, Smithson WA, Robison LL, Late mortality experience in five-year survivors of childhood and adolescent cancer: the childhood cancer survivor study. J. Clin. Oncol 19 (2001) 3163–3172. [PubMed: 11432882]

[46]. Laverdière C, Cheung NV, Kushner BH, Kramer K, Modak S, LaQuaglia MP, Wolden S, Ness KK, Gurney JG, Sklar CA. Long-term complications in survivors of advanced stage neuroblastoma. Pediatr. Blood Cancer 45 (2005) 324–332. [PubMed: 15714447]

[47]. Perwein T, Lackner H, Sovinz P, Benesch M, Schmidt S, Schwinger W, Urban C, Survival and late effects in children with stage 4 neuroblastoma. Pediatr. Blood Cancer. 57 (2011) 629–635. [PubMed: 21319289]

[48]. Bausero MA, Panoskaltsis-Mortari A, Blazar BR, Katsanis E, Effective immunization against neuroblastoma using double-transduced tumor cells secreting GM-CSF and interferon-gamma. J. Immunother. Emphasis Tumor Immunol 19 (1996) 113–124. [PubMed: 8732694]

[49]. Rousseau RF, Haight AE, Hirschmann-Jax C, Yvon ES, Rill DR, Mei Z, Smith SC, Inman S, Cooper K, Alcoser P, Grilley B, Gee A, Popek E, Davidoff A, Bowman LC, Brenner MK, Strother D, Local and systemic effects of an allogeneic tumor cell vaccine combining transgenic human lymphotactin with interleukin-2 in patients with advanced or refractory neuroblastoma. Blood 101 (2003) 1718–1726. [PubMed: 12406881]

[50]. Singh N, Kulikovskaya I, Barrett DM, Binder-Scholl G, Jakobsen B, Martinez D, Pawel B, June CH, Kalos MD, Grupp SA, T cells targeting NY-ESO-1 demonstrate efficacy against disseminated neuroblastoma. Oncoimmunology 5 (2015) e1040216. [PubMed: 26942053]

[51]. Navid F, Armstrong M, Barfield RC, Immune therapies for neuroblastoma. Cancer Biol. Ther 8 (2009) 874–882. [PubMed: 19342881]

[52]. Zenarruzabeitia O, Vitalle J, Astigarraga I, Borrego F. Natural killer cells to the attack: combination therapy against neuroblastoma. Clin. Cancer Res 23 (2017) 615–617. [PubMed: 27872101]

[53]. Spel L, Boelens JJ van der Steen DM, Blokland NJ, van Noesel MM, Molenaar JJ, Heemskerk MH, Boes M, Nierkens S. Natural killer cells facilitate PRAME-specific T-cell reactivity against neuroblastoma. Oncotarget 6 (2015) 35770–35781. [PubMed: 26452036]

[54]. Semeraro M, Rusaliewicz S, Zitvogel L, Kroemer G. Natural killer cell mediated immunosurveillance of pediatric neuroblastoma. Oncoimmunology 4 (2015) e1042202. [PubMed: 26451315]

[55]. Wang W, Erbe AK, Hank JA, Morris ZS, Sondel PM. NK cell-mediated antibody-dependent cellular cytotoxicity in cancer immunotherapy. Front. Immunol 6 (2015) 368. [PubMed: 26284063]

[56]. Rujkijyanont P, Chan WK, Eldridge PW, Lockey T, Holladay M, Rooney B, Davidoff AM, Leung W, Vong Q. Ex vivo activation of CD56(+) immune cells that eradicate neuroblastoma. Cancer Res 73 (2013) 2608–2618. [PubMed: 23440424]

[57]. Oh KT, Bronich TK, Bromberg L, Hatton TA, Kabanov AV, Block ionomer complexes as prospective nanocontainers for drug delivery. J. Controlled Release 115 (2006) 9–17.

[58]. Bronich TK, Bontha S, Shlyakhtenko LS, Bromberg L, Hatton TA, Kabanov AV, Template-assisted synthesis of nanogels from Pluronic-modified poly(acrylic acid). J. Drug Targeting. 14 (2006) 357–366.

[59]. Chander V, Gangenahalli G, Pluronic-F127/Platelet microvesicles nanocomplex delivers stem cells in high doses to the bone marrow and confers post-irradiation survival. Sci. Rep 10 (2020) 156. [PubMed: 31932650]

[60]. Wang Y, Wang Y, Wang J, Lei W, Li K, Wu D, Wang X, Pharmacokinetics, biodistributions, and bioavailability of gossypol-loaded Pluronic F127 nanoparticles. J. Drug Deliv. Sci. Technol 45 (2018) 388–396.

[61]. Shriky B, Kelly A, Isreb M, Babenko M, Mahmoudi N, Rogers S, Shebanova O, Snow T, Gough T, Pluronic F127 thermosensitive injectable smart hydrogels for controlled drug delivery system development. J. Colloid Interface Sci 565 (2020) 119–139. [PubMed: 31945671]

[62]. Wu B, Takeshita N, Wu Y, Vijayavenkataraman S, H KY, Lu WF, Fuh JYH, Pluronic F127 blended polycaprolactone scaffolds via e-jetting for esophageal tissue engineering. J. Mater. Sci. Mater. Med 29 (2018) 140. [PubMed: 30120625]

[63]. Klebe R, Ruddle F, Neuroblastoma cell culture analysis of a differentiating stem cell system. J. Cell Biol 43 (1969) 69A.

[64]. Olmstead JB, Carlson K, Klebe R, Ruddle F, Rosenbaum J, Isolation of microtubule protein from cultured mouse neuroblastoma cells. Proc. Natl. Acad. Sci. USA 65 (1970) 129–136. [PubMed: 5263744]

[65]. Lee JM, Lee M, Garon E, Goldman JW, Salehi-Rad R, Baratelli FE, Schaue D, Wang G, Rosen F, Yanagawa J, Walser TC, Lin Y, Park SJ, Adams S, Marincola FM, Tumeh PC, Abtin F, Suh R, Reckamp KL, Lee G, Wallace WD, Lee S, Zeng G, Elashoff DA, Sharma S, Dubinett SM, Phase I trial of intratumoral injection of CCL21 gene-modified dendritic cells in lung cancer elicits tumor-specific immune responses and $CD8^+$ T-cell infiltration. Clin. Cancer Res 23 (2017) 4556–4568. [PubMed: 28468947]

[66]. Gray JE, Chiappori A, Williams CC, Tanvetyanon T, Haura EB, Creelan BC, Kim J, Boyle TA, Pinder-Schenck M, Khalil F, Altiok S, Devane R, Noyes D, Mediavilla-Varela M, Smilee R, Hopewell EL, Kelley L, Antonia SJ, A phase I/randomized phase II study of GM.CD40L vaccine in combination with CCL21 in patients with advanced lung adenocarcinoma. Cancer Immunol. Immunother 67 (2018) 1853–1862. [PubMed: 30209589]

[67]. Baratelli F, Takedatsu H, Hazra S, Peebles K, Luo J, Kurimoto PS, Zeng G, Batra RK, Sharma S, Dubinett SM, Lee JM, Pre-clinical characterization of GMP grade CCL21-gene modified dendritic cells for application in a phase 1 trial in non-small cell lung cancer. J. Transl. Med 6 (2008) 38. [PubMed: 18644162]

[68]. Fang T, Li R, Li Z, Cho J, Guzman JS, Kamm RD, Ploegh HL, Remodeling of the tumor microenvironment by a chemokine/anti-PD-L1 nanobody fusion protein. Mol. Pharm 16 (2019) 2838–2844. [PubMed: 31013423]

[69]. Giteau A, Venier-Julienne MC, Marchal S, Courthaudon JL, Sergent M, Montero-Menei C, Verdier JM, Benoit JP, Reversible protein precipitation to ensure stability during encapsulation within PLGA microspheres. Eur. J. Pharm. Biopharm 70 (2008) 127–136. [PubMed: 18448319]

[70]. Moralez-Cruz M, Flores-Fernandez GM, Morales-Cruz M, Orellano EA, Rodriguez-Martinez JA, Ruiz M, Griebenow K, Two-step nanoprecipitation for the production of protein-loaded PLGA nanospheres. Results Pharma Sci 2 (2012) 79–85. [PubMed: 23316451]

[71]. Xu X, Costa A, Burgess DJ, Protein encapsulation in unilamellar liposomes: high encapsulation efficiency and a novel technique to assess lipid-protein interaction. Pharm. Res 29 (2012) 1919–1931. [PubMed: 22403024]

[72]. Sambi M, Bagheri L, Szewczuk MR, Current challenges in cancer immunotherapy: multimodal approaches to improve efficacy and patient response rates. J. Oncol (2019) Article ID 4508794.

[73]. Bronger H, Singer J, WIndmuller C, Reuning U, Zech D, Delbridge C, Dorn J, Kiechle M, Schmalfeldt B, Schmitt M, Avril S, CXCL9 and CXCL10 predict survival and are regulated by cyclooxygenase inhibition in advanced serous ovarian cancer. Br. J. Cancer 115 (2016) 553–563. [PubMed: 27490802]

[74]. Chen J, Ye X, Pitmon E, Lu M, Wan J, Jellison ER, Adler AJ, Vella AT, Wang K, IL-17 inhibits CXCL9/10-mediated recruitment of $CD8^+$ cytotoxic T cells and regulatory T cells to colorectal tumors. J. Immunother. Cancer. 7 (2019) 324. [PubMed: 31775909]

[75]. Allen F, Rauhe P, Askew D, Tong AA, Nthale J, Eid S, Myers JT, Tong C, Huang AY, CCL3 enhances antitumor immune priming in the lymph node via IFN-gamma with dependency on natural killer cells. Front. Immunol 8 (2017) 1390. [PubMed: 29109732]

[76]. Sharma S, Stolina M, Luo J, Strieter RM, Burdick M, Zhu LX, Batra RK, Dubinett SM, Secondary lymphoid tissue chemokine mediates T cell-dependent antitumor responses in vivo. J. Immunol 164 (2000) 4558–4563. [PubMed: 10779757]

[77]. Sharma S, Yang SC, Hillinger S, Zhu LX, Huang M, Batra RK, Lin JF, Burdick MD, Strieter RM, Dubinett SM, SLC/CCL21-mediated anti-tumor responses require IFNgamma, MIG/CXCL9 and IP-10/CXCL10. Mol. Cancer 2 (2003) 22. [PubMed: 12740040]

[78]. Yang SC, Hillinger S, Riedl K, Zhang L, Zhu L, Huang M, Atianzar K, Kuo BY, Bardner B, Batra RK, Strieter RM, Dubinett SM, Intratumoral administration of dendritic cells overexpressing CCL21 generates systemic antitumor responses and confers tumor immunity. Clin. Cancer Res 10 (2004) 2891–2901. [PubMed: 15102698]

[79]. Phan-Lai V, Kievit FM, Florczyk SJ, Wang K, Disis ML, Zhang M., CCL21 and IFN-γ recruit and activate tumor specific T cells in 3D scaffold model of breast cancer. Anticancer Agents Med. Chem 14 (2014) 204–210. [PubMed: 24237220]

[80]. Lode HN, Dreier T, Xiang R, Varki NM, Kang AS, Reisfeld RA, Gene therapy with a single change interleukin 12 fusion protein induces T cell-dependent protect immunity in a syngeneic model of murine neuroblastoma. Roc. Natl. Acad. Sci 95 (1998) 2475–2480.

[81]. Croce M, Meazza R, Orengo AM, Radic L, De Giovanni B, Gambini C, Carlini V, Pistoia V, Mortara L, Accolla RS, Corrias MV, Ferrini S, Sequential immunogene therapy with interleukin-12- and interleukin-15-engineered neuroblastoma cells cures metastatic disease in syngeneic mice. Clin. Cancer Res 11 (2005) 735–742. [PubMed: 15701863]

[82]. Allen F, Bobanga JD, Rauhe P, Barkauskas D, Teich N, Tong C, Myers J, Huang AY, CCL3 augments tumor rejection and enhances CD8+ T cell infiltration through NK and CD103+ dendritic cell recruitment via IFN-gamma. Oncoimmunology. 7 (2018)

[83]. Egler RA, Burlingame SM, Nuchtern JG, Russell HV. Interleukin-6 and soluble interleukin-6 receptor levels as markers of disease extent and prognosis in neuroblastoma. Clin. Cancer Res 14 (2008) 7028–7034. [PubMed: 18980999]

[84]. Lagmay JP, London WB, Gross TG, Termuhlen A, Sullivan N, Axel A, Mundy B, Ranalli M, Canner J, McGrady P, Hall B, Prognostic significance of interleukin-6 single nucleotide polymorphism genotypes in neuroblastoma: rs1800795 (promoter) and rs8192284 (receptor). Clin. Cancer Res 15 (2009) 5234–5239. [PubMed: 19671870]

[85]. Paul P, Rellinger EJ, Qiao J, Lee S, Volny N, Padmanabhan C, Romain CV, Mobley B, Correa H, Chung DH. Elevated TIMP-1 expression is associated with a prometastatic phenotype, disease relapse, and poor survival in neuroblastoma. Oncotarget 8 (2017) 82609–82620. [PubMed: 29137288]

[86]. Reinstein ZZ, Pamarthy S, Sagar V, Costa R, Adulkadir SA, Giles FJ, Carneiro BA, Overcoming immunosuppression in bone metastases. Crit. Rev. Oncol. Hematol 1177 (2017) 114–127.

[87]. Rosner S, Seng F, Postow M, Response after treatment with pembrolizumab in a patient with myelophthisis due to melanoma: the role of checkpoint inhibition in the bone. J. ImmunoTher. Cancer 5 (2017) 34. [PubMed: 28428883]

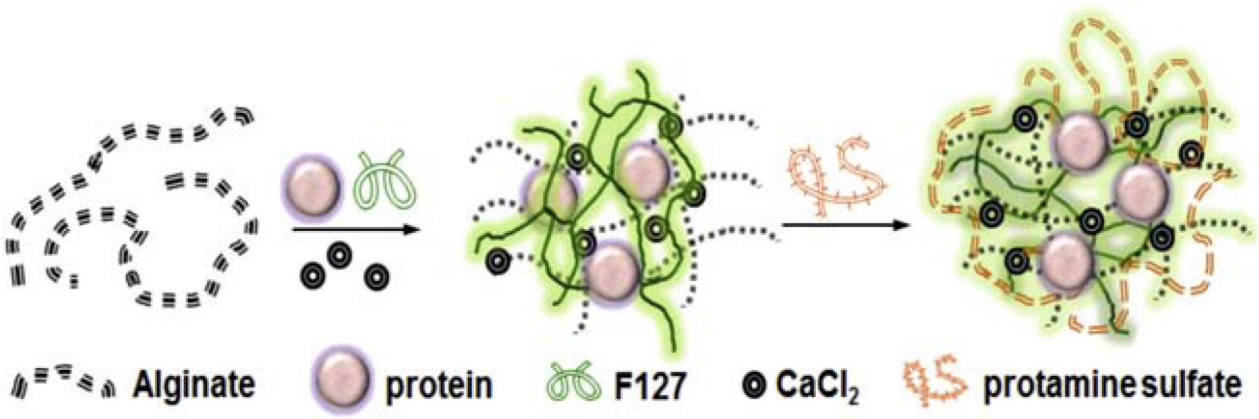

Fig. 1.

Schematic representation of the preparation of protein (cytochrome c or CCL21) - loaded alginate nanoparticles by the ionotropic gelation method. Alginate (in an aqueous solution), protein, and Pluronic F127 were combined prior to the addition of CaCl2, which induced the formation of cross-linked matrices in a pre- gelation state. The addition of Pluronic F127 strengthened the matrices of the alginate nanoparticles and prolonged the release of the protein payload. Incorporation of protamine sulfate allowed for the formation of a polyelectrolyte complex, which stabilized the alginate pre-gel nucleus into individual particles.

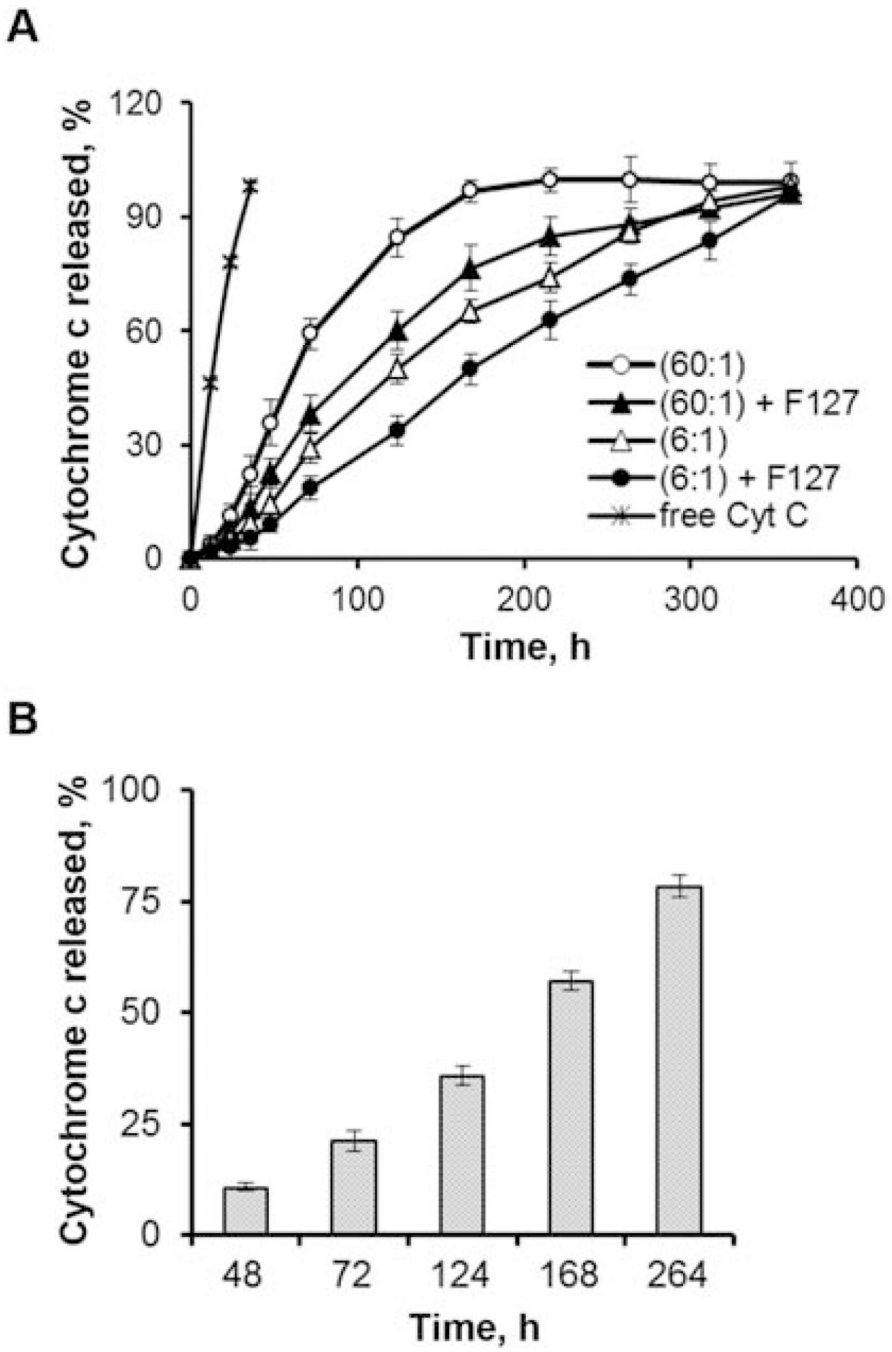

Fig. 2. Sustained release of protein cargo from the alginate nanoparticles was demonstrated.

(A) Inclusion of Pluronic F127 and reduction of the alginate : protein ratio prolonged protein cargo release from the nanoparticles. Cytochrome c release rates were determined *in vitro* to define the optimum alginate : protein ratio and impact of Pluronic FI 27 (1% w/w) inclusion in the nanoparticles. For these formulations, ratios of alginate : cytochrome c at 60:1 or 6:1 were compared, either with or without 1% Pluronic F127. All of the nanoformulations also included $CaCl_2$ and protamine sulfate. The nanoformulations, along with free cytochrome c as a control, were subjected to dynamic dialysis at 37°C, pH 7.4, and cytochrome c release

was monitored by spectrophotometric analysis of aliquots from the dialysate. Similar results were obtained in experiments repeated 4 times for the F127-containing formulations and 3 times for the formulations without F127, using freshly prepared formulations each time and making independent release measurements for each of the formulation batches. (B) Cytochrome c-loaded alginate nanoparticles (formulation alginate : cytochrome c 6:1+F127) were prepared, using 50 μg of cytochrome c for encapsulation. The nanoparticles were concentrated (5X) and resuspended in PBS (pH 7.4). The solution was divided into several 1 mL aliquots and the initial cytochrome c concentration was determined (~ 6 μg/mL). The remaining aliquots were incubated at 37°C in a water bath. At predetermined time points, the suspension was centrifuged at 10,000 rpm (30,000 × g) for 30 minutes at 4°C to separate the nanoparticle pellets and supernatants, and the concentration of cytochrome c in each of the supernatants was determined. All measurements were taken in triplicate.

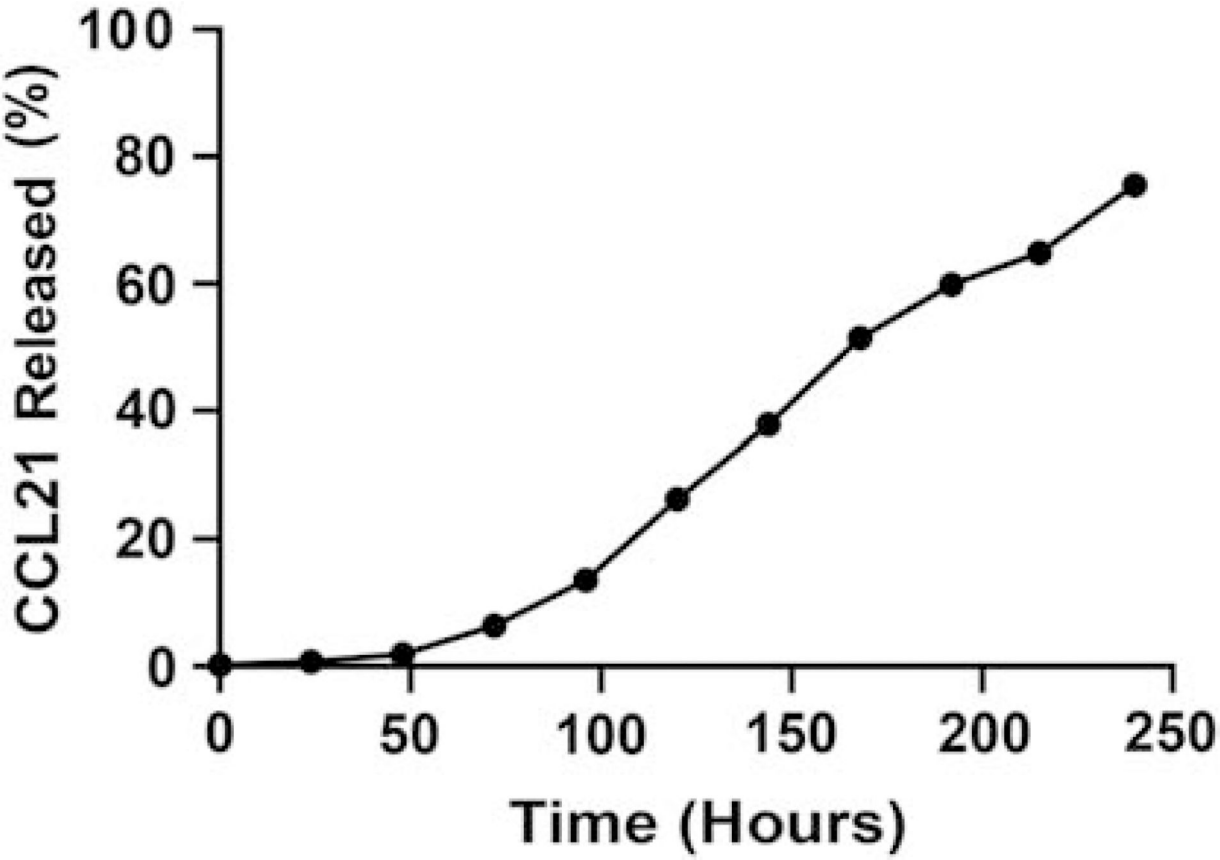

Fig. 3.

CCL21 was released from alginate nanoparticles over an extended time. The release of CCL21, from the alginate nanoparticle, was assayed by dialysis at 37°C, using PBS, pH 7.4, followed by enzyme-linked immunosorbent assay (ELISA).

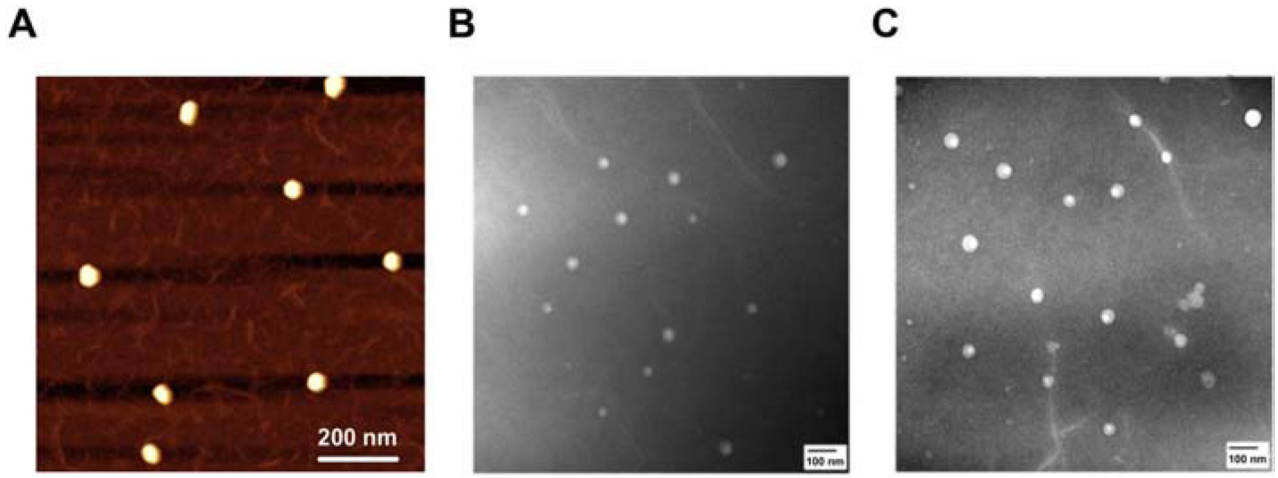

Fig. 4.

AFM and TEM demonstrated uniform, spherical alginate nanoparticle structures with minimal to no aggregation. The picture shown in (A) is a representative tapping-mode AFM image of CCL21-containing alginate nanoparticles deposited from aqueous solution onto APS-mica. The panels shown in (B) and (C) display TEM-negative staining of the empty alginate nanoparticles and CCL21-loaded nanoparticles, respectively.

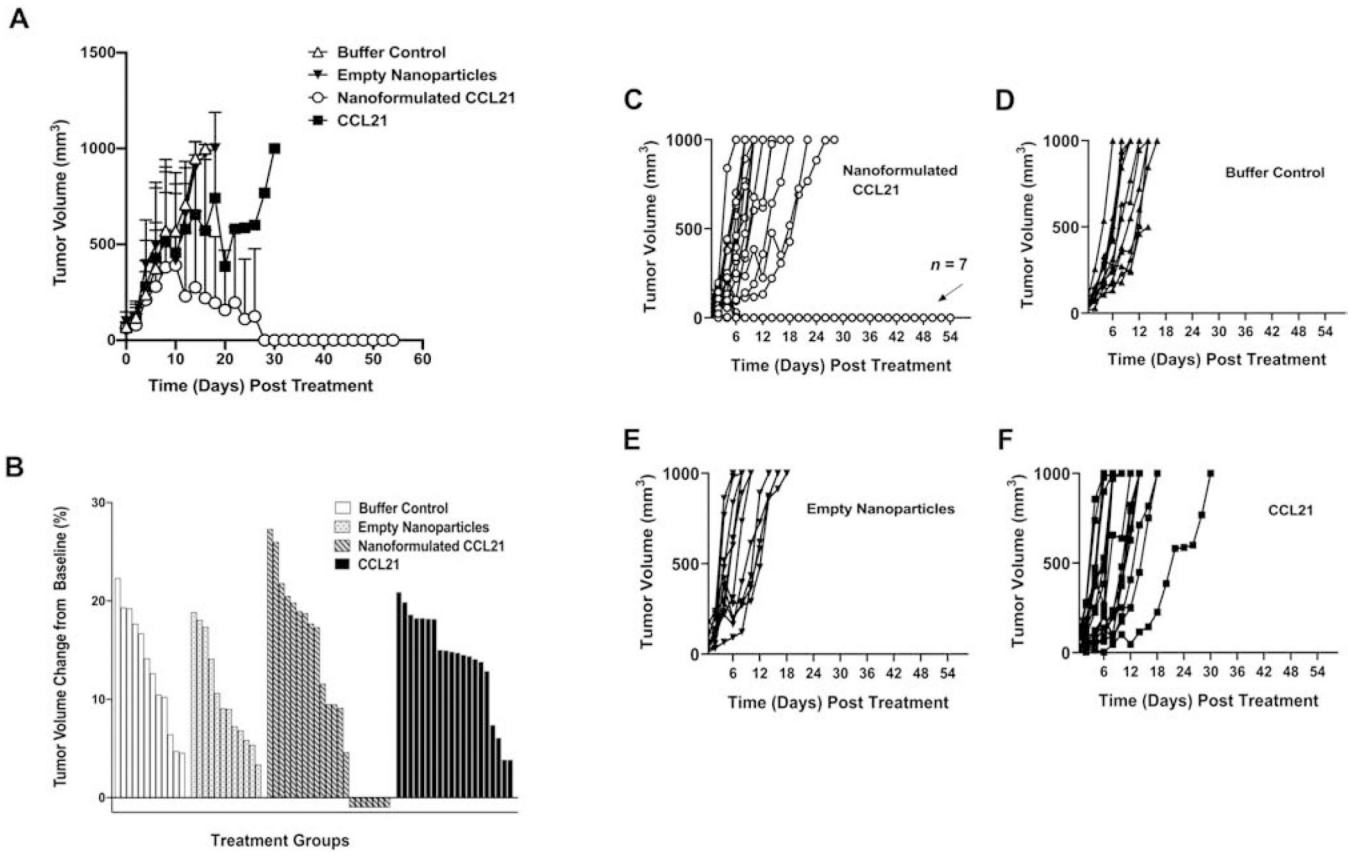

Fig. 5.

Intratumoral treatment with nanoformulated CCL21 caused complete regression in 7 out of 21 Neuro2a tumor-bearing mice treated with nanoformulated CC21, and the average tumor growth was slower for nanoformulated CCL21-treated mice compared to controls. Tumors were initiated by subcutaneous injection of 1 X 10^6 Neuro2a cells/100 μL PBS into the lower right flank, allowed to grow until palpable, and then treated as described in Section 2. Materials and methods. Tumor-bearing mice received twice daily injections (1 dose in the morning and 1 dose in the evening) for 2 consecutive days delivering 6 μg of CCL21/25 μL, or 6 μg of CCL21 in nanoformulation/25 μL, or an equal amount of empty nanoparticles/25 μL, or an equal volume (25 μL) of buffer (diagrammed in Fig. S1). (A) Average tumor volumes over time are shown for mice treated with buffer control, empty nanoparticles, nanoformulated CCL21, or CCL21. The tumor growth rate was significantly slower for nanoformulated CCL21-treated mice ($p < 0.001$) as compared to mice that were administered buffer control, empty nanoparticles, or CCL21 alone. Tumors were measured in 2 perpendicular directions with a caliper at least 3 times weekly. Tumor volumes were calculated as tumor width^2 X tumor length/2, and they were averaged across treatment groups and compared using Linear Mixed Models analysis. The bars represent standard deviation. Mice were euthanized if the tumor volume reached 1000 mm^3. The data shown are a cumulative representation of 3 independent experiments. (B) Percent change in tumor volume from baseline was calculated via the following formula (final tumor volume – initial tumor volume)/initial tumor volume X 100, where the final tumor volume was 1000 mm^3 or the tumor volume at 54 days post treatment initiation. If a tumor failed to be detected via

palpation or necropsy at day 54 post treatment initiation, a tumor volume of 0 mm^3 was entered as the final volume. The initial tumor volume (day 0) was set as the baseline and is indicated graphically as 0%. Tumors that had smaller initial volumes (~50 mm^3) showed the greatest percent change from baseline while tumors with slightly larger volumes demonstrated smaller percent changes. All treatment groups exhibit positive changes in tumor growth from baseline, which indicates increasing tumor volume over time following treatment initiation. Most notably, only nanoformulated CCL21 therapy was able to induce complete tumor regression in a subset of mice (n = 7). The regressed subset is graphically depicted as a negative percent (−100%) due to the tumor shrinking past a palpable stage and failure to be detected upon necropsy. Therefore, the change in tumor volume from baseline in mice with regressed tumors was found to be −100 %. (C, D, E, F) The changes in tumor volumes for each mouse treated with (C) nanoformulated CCL21, (D) buffer control, (E) empty nanoparticles, or (F) CCL21 alone are shown. After treatment, the mice were monitored and their tumors were measured at least 3 times weekly until their tumor burdens reached 1000 mm^3, and the mice with regressed tumors were monitored until day 54.

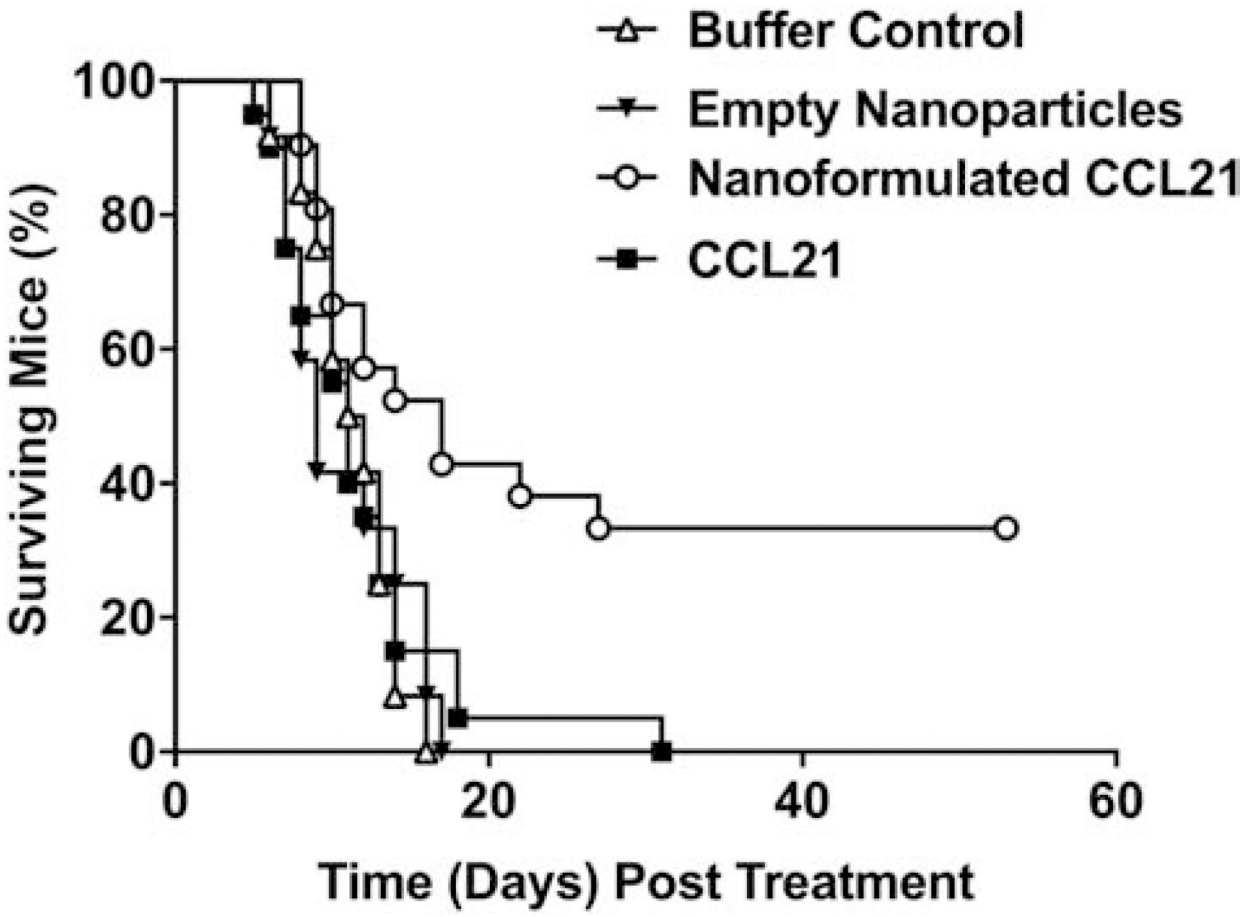

Fig. 6.

Survival distributions of tumor-bearing mice were significantly prolonged by nanoformulated CCL21 treatment. A/J mice bearing subcutaneous Neuro2a neuroblastoma tumors received intratumoral injections with one of the following agents: nanoformulated CCL21 (n=21), CCL21 alone (n=20), empty nanoparticles (n=12), or buffer control (n=12). The Neuro2a tumor-bearing mice were given 1 dose in the morning and 1 dose in the evening on 2 consecutive days of 6 μg of CCL21/25 μL, or 6 μg of CCL21 in nanoformulation/25 μL per dose, or an equal amount of empty nanoparticles/25 μL, or 25 μL of buffer alone (Fig. S1). After receiving the treatments, the mice were monitored at least 3 times weekly until their tumor burdens reached 1000 mm^3 or 54 days had elapsed since treatment initiation (day 0). Nanoformulated CCL21-treated mice survived significantly longer than mice treated with buffer control ($p = 0.008$), empty nanoparticles ($p = 0.002$), or CCL21 alone ($p = 0.003$). Kaplan-Meier and log-rank analyses were used to compare survival distributions of mice between treatment groups. Survival distributions were generated using Kaplan-Meier Survival Methods and portray cumulative survival in time (days), where day 0 indicates treatment initiation, not the implantation of tumor cells. Mean survival time post-treatment initiation ± standard deviation was determined for each treatment group. These data are a cumulative representation of 3 independent experiments.

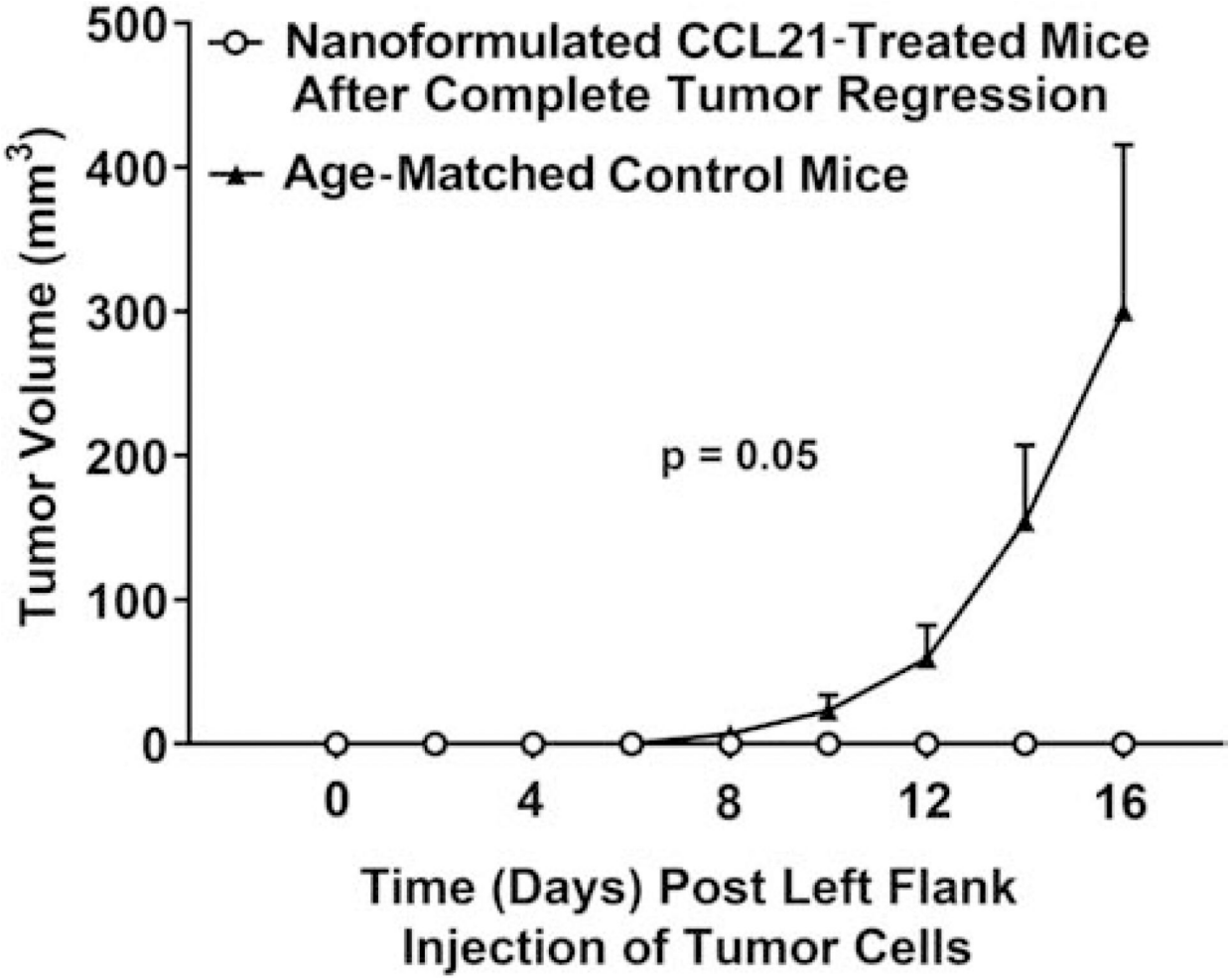

Fig. 7.

Systemic, protective, antitumor responses were observed in a subset of nanoformulated CCL21-treated mice, a phenomenon not seen with the other treatments tested. As described in the Fig. 6 legend and diagrammed in Fig. S1, Neuro2a tumor-bearing mice were administered 2 doses (1 in a.m. and 1 in p.m.) on 2 consecutive days of 6 μg of CCL21/25 μL, or 6 μg of CCL21 in nanoformulation/25 μL per dose, or an equal amount of empty nanoparticles/25 μL, or 25 μL of buffer alone. From the mice for which data are shown in Fig. 6, the subset of cured, nanoformulated CCL21-treated mice (tumor free at day 54, n = 7) were rechallenged with subcutaneous injection of 1 X 10^6 Neuro2a cells/100 μL PBS into the lower left flank (opposite to the initial site of Neuro2a cell injection and intratumoral treatment). A group of treatment naïve, age- and sex-matched A/J mice were challenged in parallel. The cured, nanoformulated CCL21-treated, rechallenged mice failed to develop tumors by the experimental end point (day 70), unlike their age-matched, treatment naïve counterparts, which developed palpable, steadily growing tumors. The graph displays tumor growth over time, with the challenge (second challenge for cured mice, initial challenge for treatment naïve, age matched controls) date indicated as day 0. The tumors were measured in 2 perpendicular directions using a caliper at least 3 times weekly. Tumor volumes were calculated as tumor width^2 X tumor length/2, averaged across treatment groups, and

compared using Linear Mixed Models analysis. The bars represent the standard error of the mean. The data shown consist of a cumulative representation of 3 independent experiments.

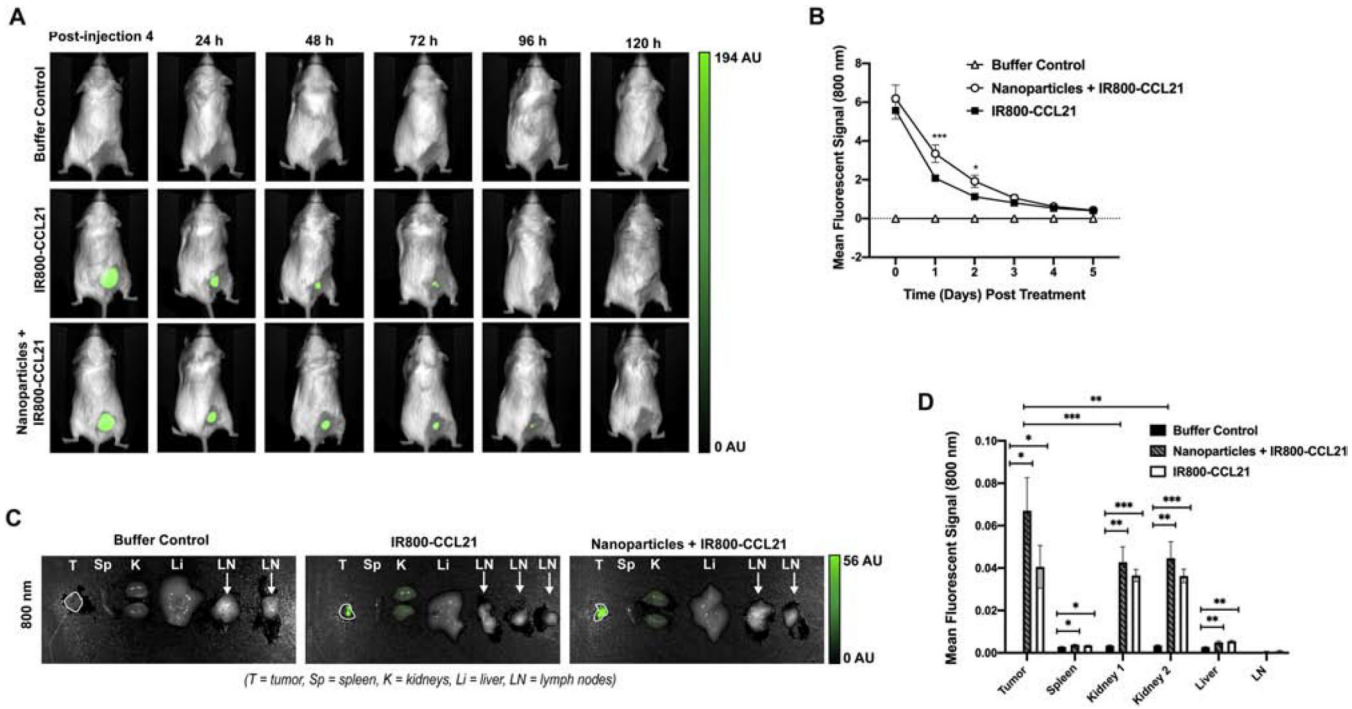

Fig. 8.

Fluorescently labeled CCL21 delivered to neuroblastoma tumors in nanoparticles was found to be present at a higher level at day 1 and day 2 following treatment, as compared to fluorescently labeled CCL21 delivered alone. Each of 3 mouse groups received twice daily injections (1 dose in the morning and 1 dose in the evening) for 2 consecutive days, with the injections consisting of 25 μL per dose of buffer control, IR800-CCL21, or Nanoparticles + IR800-CCL21, respectively (Fig. S1). Imaging was performed with the day 0 imaging done immediately after the final treatment injection, and imaging was then repeated once daily for 5 consecutive days. The mean fluorescent signal of IR800 dye was visualized in the 800 nm channel by the Pearl Trilogy Small Animal Imaging System. (A) Representative images of treated mice are shown. (B) Mice receiving the Nanoparticles + IR800-CCL21 (nanoformulated CCL21) demonstrated the highest mean intratumoral fluorescent signal over time, with significantly higher fluorescent intensity at day 1 ($p = 0.0005$) and day 2 ($p = 0.0241$) when compared to the IR800-CCL21-treated mice. The mean fluorescent signal was marginally ($p = 0.0810$) higher at day 0 in mice treated with the Nanoparticles + IR800-CCL21. Two-way ANOVA analysis was used to assess differences in the intratumoral mean fluorescent signal *in vivo* at 800 nm. (C) Imaging of fluorescently labeled CCL21 delivered in nanoparticles (Nanoparticles + IR800-CCL21) and fluorescently labeled CCL21 (IR800-CCL21) within neuroblastoma tumors, as well as in various organs (spleen, kidney, liver, and lymph nodes), was performed at the time of necropsy, 5 days post-treatment initiation, using the Pearl Trilogy Small Animal Imaging System. (D) Nanoparticles + IR800-CCL21-treated mice exhibited a trend towards the highest mean fluorescent signal in the 800 nm channel in the tumor, spleen, and kidney specimens. Minimal signal in the liver, lymph nodes, and spleen indicate that the fluorescently labeled CCL21 (either alone or in nanoformulation) is cleared through the kidneys following intratumoral administration. Two-

way ANOVA analysis was used to assess differences in the mean fluorescent signal (800 nm) of organs from mice treated with Nanoparticles + IR800-CCL21, IR800-CCL21, and buffer control. Statistical significance is defined as $p < 0.05$*, $p < 0.01$**, $p < 0.001$***, and $p < 0.0001$****.

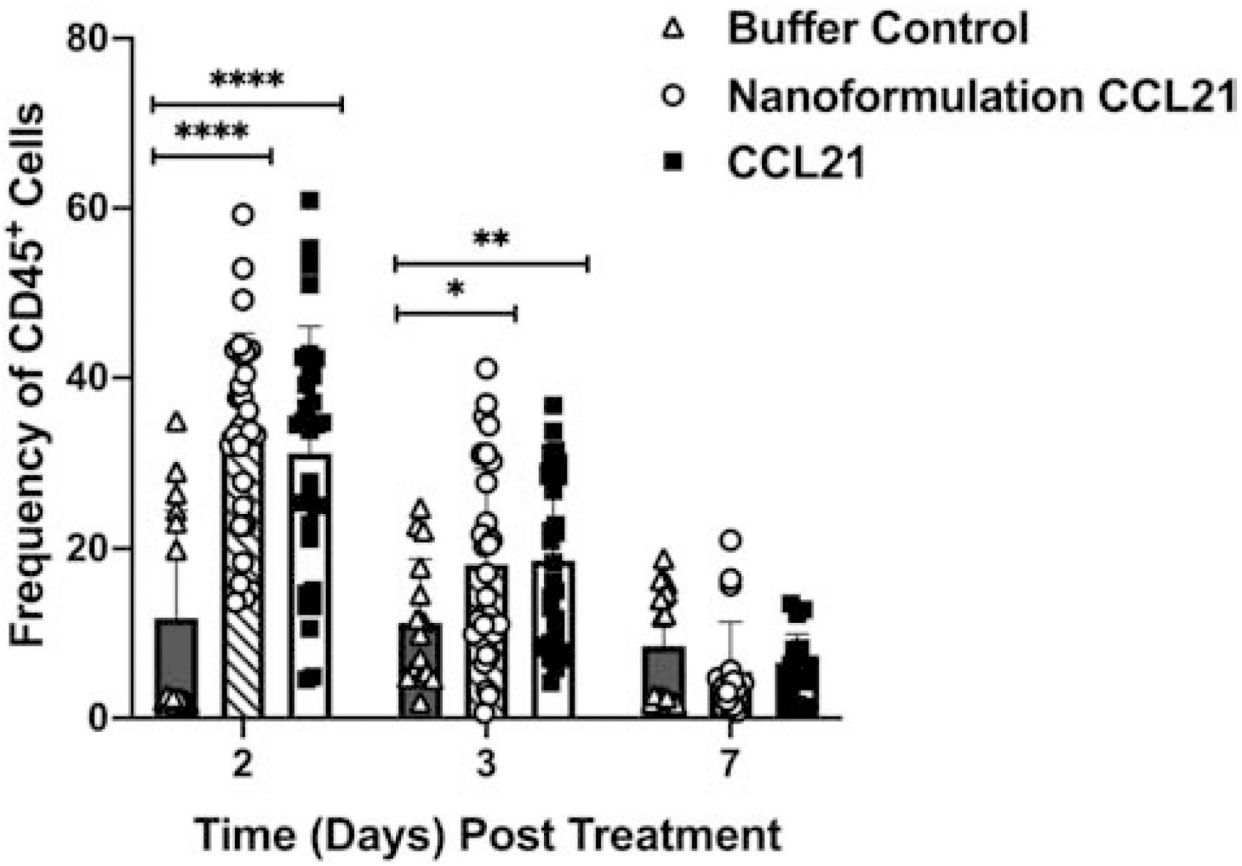

Fig. 9.

Elevated frequencies of $CD45^+$ cells were observed in tumors treated with either nanoformulated CCL21 or CCL21 in comparison to the control. Neuro2a tumor-bearing mice received 2 daily injections (1 in the morning and 1 in the evening) for 2 days in a row with each injection containing 6 μg of CCL21/25 μL, or 6 μg of CCL21 in nanoformulation/25 μL per dose, or an equal volume (25 μL) of buffer. The frequency of $CD45^+$ cells was significantly ($p < 0.0001$) higher in tumors treated with either nanoformulated CCL21 or CCL21 compared to those treated with buffer control at day 2 post treatment initiation. Significantly higher percentages of $CD45^+$ cells were also seen at day 3 post treatment in nanoformulated CCL21-treated tumors ($p = 0.0190$) or CCL21-treated tumors ($p = 0.0090$) compared to the control. Gating strategy for $CD45^+$ cells: single cells, live cells, $CD45^+$. Frequency was calculated as % marker = (number of cells that were marker positive) / (number of live cells) X 100. Graphical representation of the data depicts the mean frequency overlaid with individual data points for each group. Statistical comparisons were made via two-way ANOVA. The bars indicate standard deviation. Statistical significance was defined as $p < 0.05$*, $p < 0.01$**, $p < 0.001$***, and $p < 0.0001$****. Groups consisted of 5–10 mice per treatment group per time point.

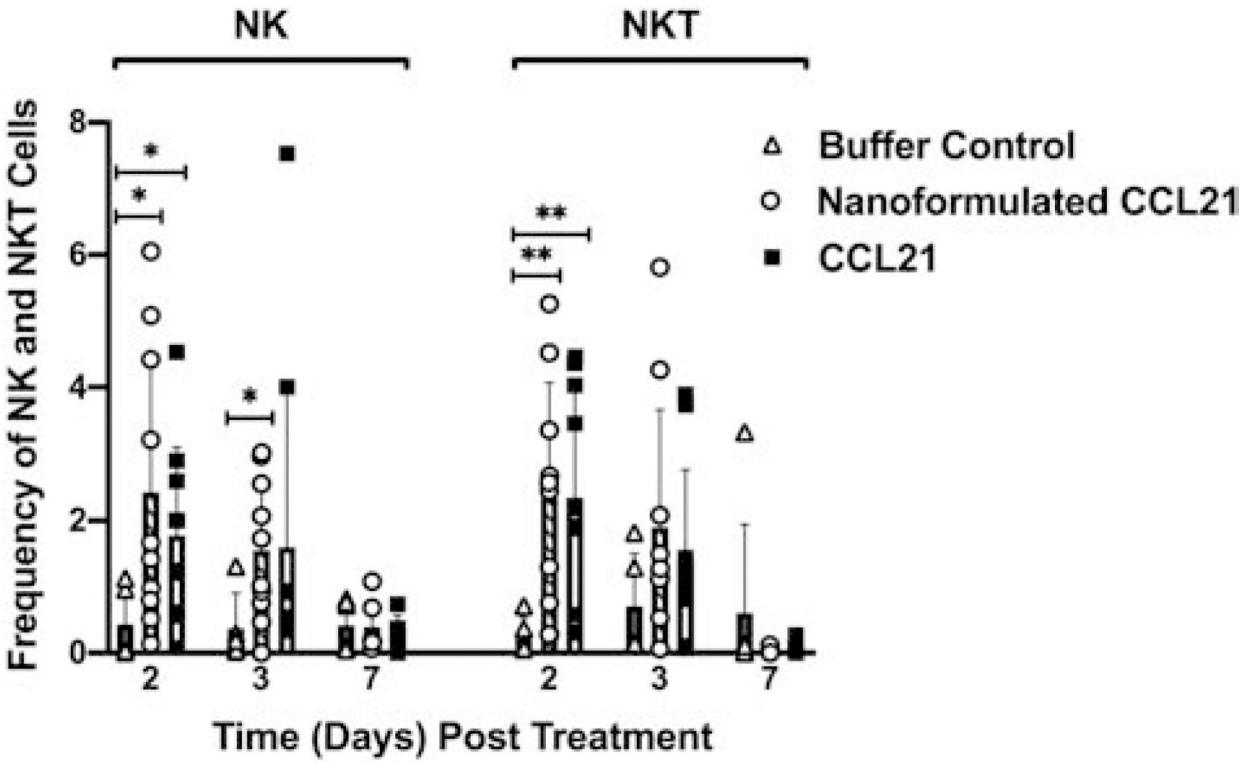

Fig. 10.

Intratumoral injection of nanoformulated CCL21 and CCL21 alone resulted in increased frequencies of NK and NKT cells. Mice with Neuro2a tumors received 2 daily injections (1 in the morning and 1 in the evening) for 2 consecutive days with each injection having 6 μg of CCL21/25 μL, or 6 μg of CCL21 in nanoformulation/25 μL per dose, or an equal volume (25 μL) of buffer. (A) NK cell frequency was significantly higher in tumors treated with nanoformulated CCL21 ($p = 0.0168$) or CCL21 ($p = 0.0169$) in comparison to the control at day 2 post treatment. Sustained augmentation of NKT cell frequencies within treated tumors was observed in the nanoformulated CCL21 ($p = 0.0039$; day 2) and CCL21 ($p = 0.0029$; day 2) groups versus tumors treated with buffer control. (B) Intragroup comparisons, from day 2 to day 7, reveal a significant loss in the frequency of NK cells within the tumor in nanoformulated CCL21-treated ($p = 0.0384$) and CCL21-treated ($p = 0.0244$) groups. Tumors treated with buffer control remained relatively low throughout the duration of the study. (C) The percentage of NKT cells per live cells was higher at day 2 post treatment and demonstrated a decrease over time. There was a significant reduction in NKT frequency from day 2 to day 7 in the nanoformulated CCL21-treated ($p = 0.0270$) and CCL21-treated ($p = 0.0191$) group. However, a majority of buffer control mice had a small percentage of NKT cells within the tumor. NK and NKT cells were determined using the following gating strategy: $CD45^+$, $CD3^{+/-}$, $CD49b^+$, with NK cells being $CD3^-$ and NKT cells being $CD3^+$. Frequency was calculated as % marker = (number of cells that were marker positive) / (number of live cells) X 100. Graphical representation of the data depicts the mean frequency overlaid with individual data points for each group. Statistical comparisons were made via two-way ANOVA. The bars indicate standard deviation. Statistical significance

was defined as $p < 0.05$* and $p < 0.01$**. Groups consisted of 5–10 mice per treatment group per time point.

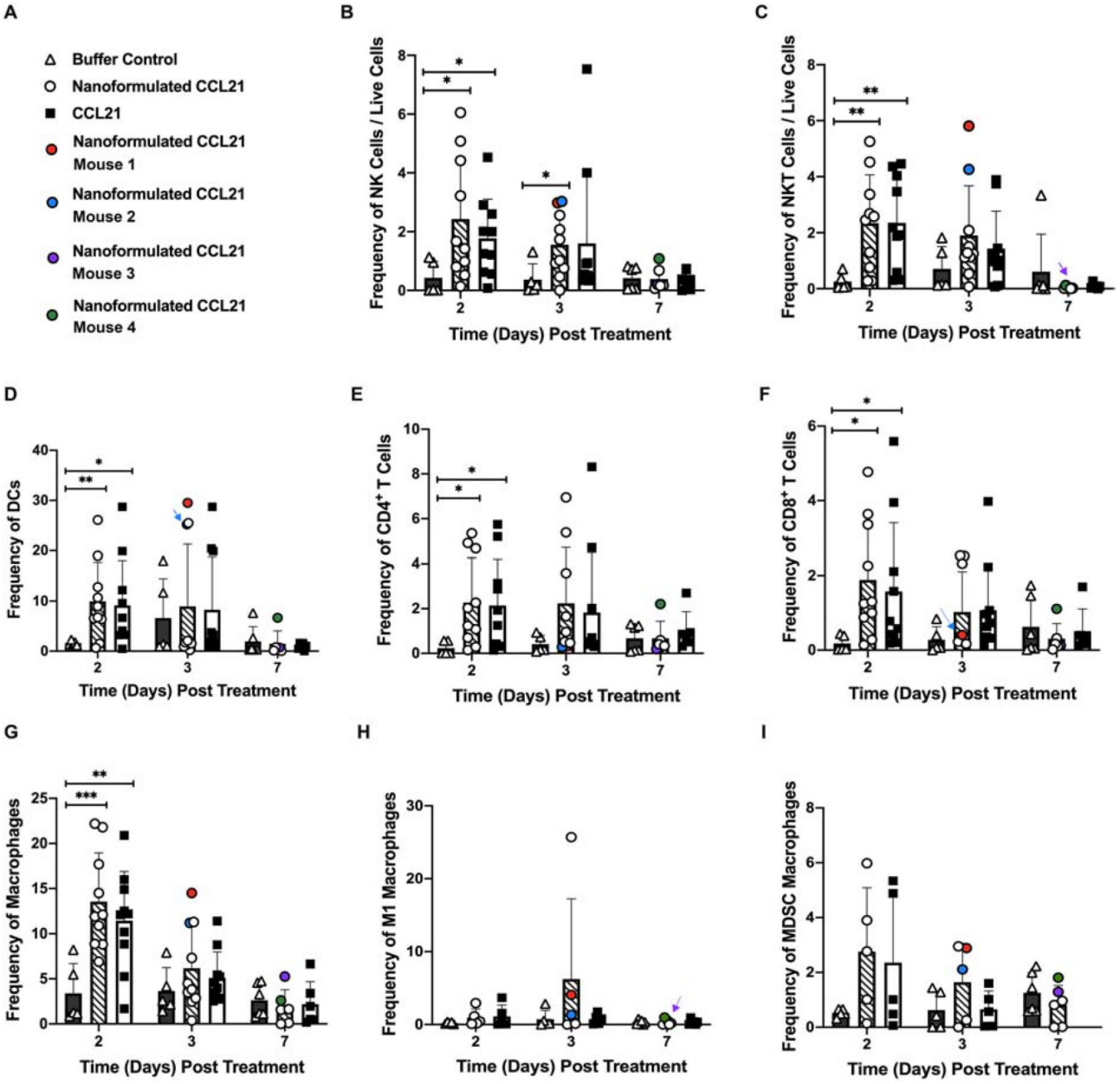

Figure 11.

Comparisons of intratumoral immune cell subset frequencies across treatment groups over time are shown, with the mice that underwent complete regression during this experiment highlighted in color (the coding key is shown in A). Neuro2a tumor-bearing mice received 2 daily intratumoral injections (1 in a.m.; 1 in p.m.) for 2 days in a row with each injection having 6 μg of CCL21/25 μL, or 6 μg of CCL21 in nanoformulation/25 μL per dose, or an equal volume (25 μL) of buffer. Frequency was calculated as % marker = (number of cells that were marker positive) / (number of live cells) X 100. Graphical representation of the data depicts the mean frequency overlaid with individual data points for each group. Statistical comparisons were made via two-way ANOVA. The bars indicate standard deviation. Statistical significance was defined as $p < 0.05$*, $p < 0.01$**, and $p < 0.001$***.

Groups consisted of 5–10 mice per treatment group per time point. The data shown in Fig. 11B and Fig. 11C are the same as that shown in Fig. 10 except that color coding has been added to Fig. 11B/C to indicate the NK and NKT intratumoral infiltration for specific mice.

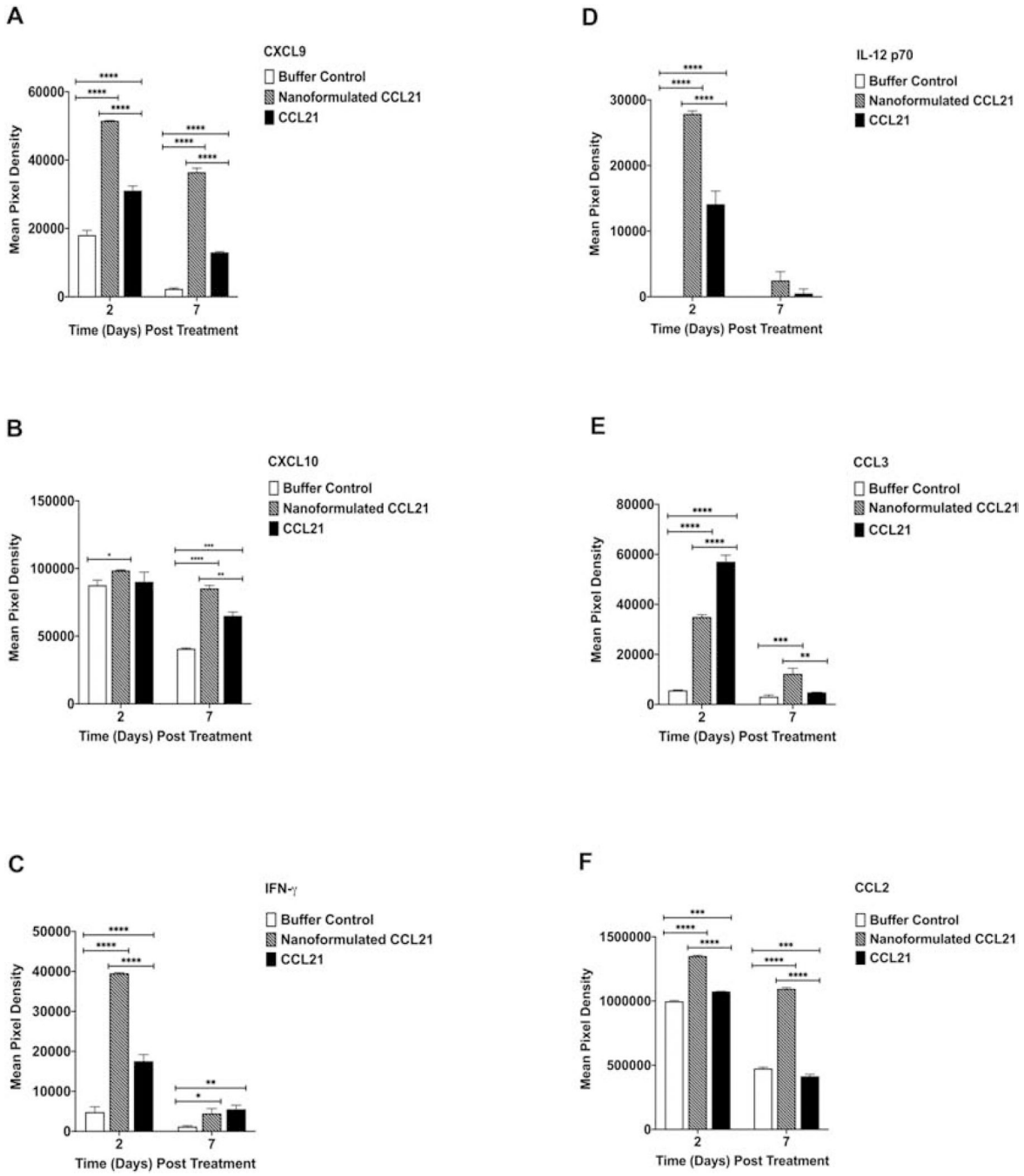

Figure 12.

In total, the intratumoral cytokine profile induced by nanoformulated CCL21 treatment, as compared to CCL21 treatment, favored increased anti-tumor cytokine expression. Neuro2a tumor-bearing mice received 2 intratumoral injections (1 in a.m.; 1 in p.m.) for 2 days in a row with each injection consisting of 6 μg of CCL21/25 μL, or 6 μg of CCL21 in nanoformulation/25 μL per dose, or an equal volume (25 μL) of buffer. Cytokine profiles from neuroblastoma tumor biopsy culture supernatants were assessed via Proteome Profiler Cytokine Array. Mean pixel densities are shown for (A) CXCL9, (B) CXCL10, (C) IFN-γ,

(D) IL-12 p70, (E) CCL3, and (F) CCL2. Statistical comparisons were made via two-way ANOVA. The bars indicate standard deviation. Statistical significance was defined as $p < 0.05$*, $p < 0.01$**, $p < 0.001$***, and $p < 0.0001$****. Groups consisted of 5 mice per treatment group per time point.

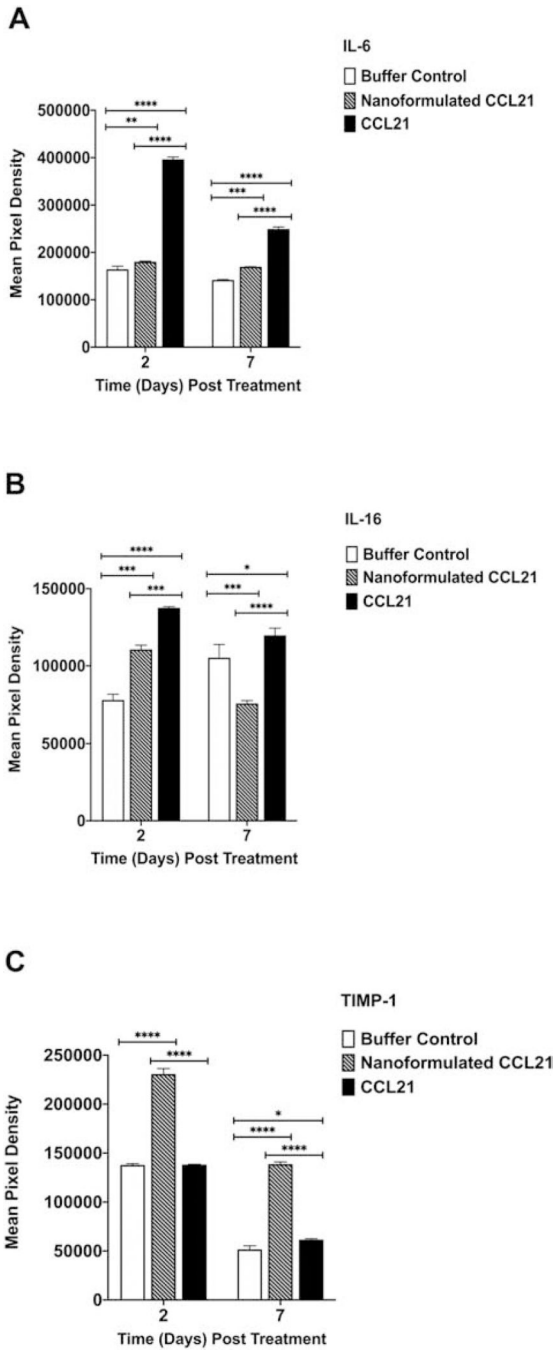

Figure 13.

The intratumoral cytokine profile induced by nanoformulated CCL21 treatment, as compared to CCL21 treatment decreased the expression of pro-tumor cytokines IL-6 and IL-16, but elevated the expression of TIMP-1. Neuro2a tumor-bearing mice were given 2 injections (1 in a.m.; 1 in p.m.) for 2 days consecutively with each injection having 6 μg of CCL21/25 μL, or 6 μg of CCL21 in nanoformulation/25 μL per dose, or an equal volume (25 μL) of buffer. Cytokine profiles from neuroblastoma tumor biopsy culture supernatants were assessed via Proteome Profiler Cytokine Array. Mean pixel densities are shown for (A) IL-6,

(B) IL-16, (C) TIMP-1. Statistical comparisons were made via two-way ANOVA. The bars indicate standard deviation. Statistical significance was defined as $p < 0.05$*, $p < 0.01$**, $p < 0.001$***, and $p < 0.0001$****. Groups consisted of 5 mice per treatment group per time point.

Table 1.

Physicochemical characteristics of alginate nanoparticles

Formulation	DLS[a]			FFF[b]	NTA[c]	AFM[d]	TEM[e]	Cryo-TEM[f]
	D_{eff} (nm)	PDI	ζ-potential (mV)	D_H (nm)	$(D_H)_n$ (nm)	D_{av} (nm)	D_{av} (nm)	D_{av} (nm)
Empty NPs	176 ± 5	0.18	−1.9 ± 1.1	172 ± 4	173 ± 11	54 ± 3	49 ± 2	163 ± 11
NPs / cyt c	164 ± 1	0.11	−0.8 ± 1.4	158 ± 6	161 ± 7	59 ± 4	51 ± 3	157 ± 8
NPs / CCL21	158 ± 3	0.16	−1.5 ± 0.6	-	179 ± 8	50 ± 2	47 ± 2	-

[a] Particle size (D_{eff}), particle size distribution (PDI) and ζ-potential were determined by DLS (1 mg/mL, PBS, pH 7.4, 25°C). Data presented as means ± SD (n = 3–5).

[b] Hydrodynamic diameter (D_H) was determined by FFF-DLS at a concentration of 1.35 mg/mL (PBS, pH 7.4, 25°C).

[c] Number-averaged hydrodynamic diameler $(D_H)_n$ was determined by NTA. Samples were diluted with PBS to a final concentration of 0.1 mg/mL prior measurements.

[d] Samples were diluted with distilled water to a final concentration of 0.01 mg/mL.

[e,f] The TEM measurements were done at alginate concentration of 2 mg/mL.